

# A retinal code for motion along the gravitational and body axes

Shai Sabbah<sup>1</sup>, John A. Gemmer<sup>2</sup>, Ananya Bhatia-Lin<sup>1</sup>, Gabrielle Manoff<sup>1</sup>, Gabriel Castro<sup>1</sup>, Jesse K. Siegel<sup>1</sup>, Nathan Jeffery<sup>3</sup> & David M. Berson<sup>1</sup>

**Self-motion triggers complementary visual and vestibular reflexes supporting image-stabilization and balance. Translation through space produces one global pattern of retinal image motion (optic flow), rotation another. We examined the direction preferences of direction-sensitive ganglion cells (DSGCs) in flattened mouse retinas *in vitro*. Here we show that for each subtype of DSGC, direction preference varies topographically so as to align with specific translatory optic flow fields, creating a neural ensemble tuned for a specific direction of motion through space. Four cardinal translatory directions are represented, aligned with two axes of high adaptive relevance: the body and gravitational axes. One subtype maximizes its output when the mouse advances, others when it retreats, rises or falls. Two classes of DSGCs, namely, ON-DSGCs and ON-OFF-DSGCs, share the same spatial geometry but weight the four channels differently. Each subtype ensemble is also tuned for rotation. The relative activation of DSGC channels uniquely encodes every translation and rotation. Although retinal and vestibular systems both encode translatory and rotatory self-motion, their coordinate systems differ.**

DSGCs encode visual motion. Earlier work has probed how they do so<sup>1–9</sup>. Here, we relate global patterns of direction preference to visual reafference during self-motion. When animals move, visual and vestibular feedback drive postural adjustments, image-stabilizing eye and head movements, and cerebellar learning<sup>10</sup>. Self-motion can be decomposed into translatory and rotatory elements—movement along, or rotation about, an axis. The vestibular apparatus achieves this biomechanically. The relative activation of otolithic organs and semicircular canals uniquely encodes every translation or rotation<sup>11</sup>.

Movement through space also produces global patterns of retinal image motion called optic flow. Translation (Fig. 1a) induces optic flow that diverges from a point in space around the mouse ('direction of heading'; asterisk in Fig. 1a), follows lines of longitude in global visual space, and converges at a diametrically opposed singularity. Rotary optic flow follows lines of latitude, circulating around a point in visual space (Fig. 1b). These motion trajectories are imaged on the hemispheric retinal surface (Fig. 1c, d). Rotatory and translatory optic flows evoke different behaviours, implying divergent encoding mechanisms and output circuits.

DSGCs encode optic flow locally within small receptive fields<sup>12</sup> (about 1% of the monocular field; Fig. 1c, red circle). Most belong to two canonical classes—ON-DSGCs and ON-OFF-DSGCs—differing in gene expression, structure, projections, functional properties and roles<sup>1</sup>.

ON-OFF-DSGCs innervate retinotopic targets mediating gaze shifts and conscious motion perception<sup>13–15</sup>. They comprise four subtypes, each preferring one of four cardinal directions<sup>16–18</sup>. The polar distribution of directional preferences among ON-OFF-DSGCs appears cruciform, with four lobes separated by 90° (Fig. 1k).

How do the directional preferences of ON-OFF-DSGCs relate to the spherical geometry of optic flow? If the cruciform pattern is universal, as widely assumed, a surprising corollary follows: one pair of subtypes must prefer motion along meridians as in translatory optic flow (Fig. 1a), while the other pair follows orthogonal lines of latitude, like rotatory flow (Fig. 1b). The dorsal/ventral pair matches translatory flow

in Fig. 1e, f, but could match rotatory flow instead, provided the nasal/temporal pair also switches, to translatory flow.

By intensive global mapping of direction selectivity (DS), we refute this model. Instead, we find that all four ON-OFF-DSGC subtypes align their preferences everywhere with one of four cardinal translatory optic flow fields, thereby encoding self-motion along two specific axes—the gravitational and body axes. Each subtype forms a panoramic, binocular ensemble best activated when the animal rises, falls, advances or retreats. We expected the other DSGC class—ON-DSGCs—would exhibit a distinct geometry (Supplementary Note 1). Surprisingly, they proved to adhere to the same translatory optic-flow geometry as ON-OFF-DSGCs, and to comprise four subtypes, not three<sup>18,19</sup>. Though optimally tuned for translatory flow, DSGC ensembles also respond differentially to rotatory flow. Any translation or rotation is uniquely encoded in the relative activation of these channels, permitting the brain to differentiate translation from rotation by simple global summation or subtraction of channels.

## Mapping global direction preferences of DSGCs

We mapped the direction preferences of >2,400 DSGCs at known locations in flattened mouse retinas *in vitro* (from >33,900 neurons; 26 retinas; Fig. 1g, h). DSGCs were identified from Ca<sup>2+</sup> responses to moving stimuli, imaged by two-photon microscopy of virally expressed GCaMP6f (Methods; Extended Data Fig. 1a–d). All were ganglion cells (immunopositive for RNA-binding protein with multiple splicing<sup>20</sup>;  $n = 706$ ; Extended Data Fig. 2a–f). ON-OFF-DSGCs were discriminated from ON-DSGCs by unsupervised clustering (Gaussian mixture models, Methods), exploiting their faster, more transient ON responses (Extended Data Fig. 3a–h). ON-OFF-DSGCs greatly outnumbered ON-DSGCs (ON-OFF:  $n = 1,949$ ;  $6.6\% \pm 2.1\%$  of imaged cells per retina versus ON:  $n = 497$ ;  $1.8\% \pm 0.9\%$ ; mean  $\pm$  s.d., Supplementary Note 2). No OFF-DSGCs were encountered. Each cell's location was mapped to spherical coordinates, permitting comparisons across retinas using standardized displays as projected or flattened spherical surfaces (Extended Data Fig. 4, Supplementary Equations).

<sup>1</sup>Department of Neuroscience, Brown University, Providence, Rhode Island 02912, USA. <sup>2</sup>Department of Mathematics and Statistics, Wake Forest University, Winston-Salem, North Carolina 27109, USA. <sup>3</sup>Institute of Ageing and Chronic Disease, University of Liverpool, Liverpool L69 3GA, UK.

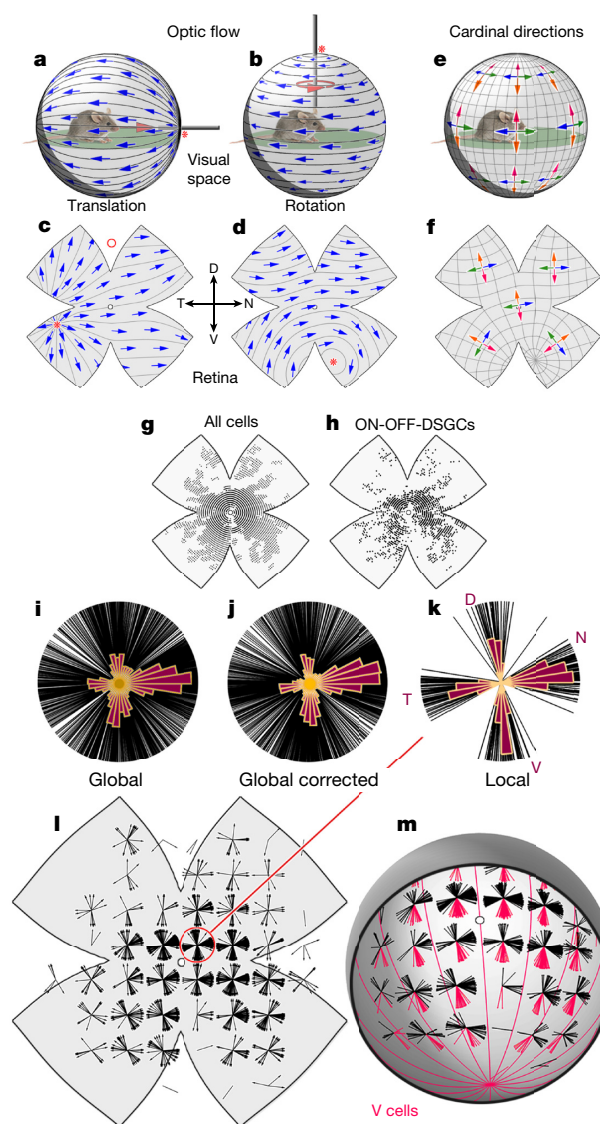


**Figure 1 | Directional preferences of ON-OFF-DSGCs are topographically dependent.** a–d, Optic flow induced by animal's translation (a, c) or rotation (b, d) (pink arrows) and illustrated as apparent motions (blue arrows) in the visual space around the animal (a, b) and projected onto the retina, after flattening (c, d). Asterisks, flow fields' centre of expansion (a, c) or rotation (b, d). Red circle in c, DSGC receptive-field size. N, nasal; D, dorsal; T, temporal; and V, ventral. e, f, Inferred geometry of ON-OFF-DSGC preferences assuming cardinal directions remain orthogonal everywhere. One pair of subtypes (orange, red) follow longitudinal (translatory-flow) geometry, the other (blue, green) latitudinal (rotatory-flow) geometry. g, h, Location of calcium-imaged cells (g) and imaged ON-OFF-DSGCs (h). i–k, Polar plots of DS preference among imaged ON-OFF-DSGCs, one line per cell. Polar histograms are overlaid. Cells pooled from whole retina (i, j) or only from the small circled central region (k). l, Topographic dependence of ON-OFF-DSGC local directional preferences, displayed as polar plots on a standardized flattened retinal map. m, Same as l but in reconstructed 3D view, corrected for histological distortions. Cells preferring ventral retinal movement (red lobes; 'V-cell' subtype) prefer motion towards a ventral singularity (centre of contraction) and align with optic flow produced by downward translation (red meridians in m; compare pink arrows in e, f).

### ON-OFF-DSGCs prefer translatory optic flow fields

Like all imaged cells, ON-OFF-DSGCs were widely distributed but concentrated centrally owing to preferential viral infection (Fig. 1g, h). Their DS preferences, pooled across retinas and displayed in polar format, were markedly disordered (Fig. 1i). Four lobes marking

the cardinal directions were apparent, but broad and blurred, without expected gaps. Correcting errors in retinal orientation (Fig. 1j) did not resolve this (Extended Data Fig. 5e). The disorder derived instead mainly from systematic topographic variation in DS preferences. Four distinct lobes emerged when sampling only central retina (Fig. 1k), but elsewhere the lobes tilted relative to cardinal retinal directions and one another (Fig. 1l). Such topographic dependence is not an artefact of retinal flattening; it is even more apparent when viewed in reconstructed three-dimensional form (Fig. 1m). Thus, plots of DS preference are not ubiquitously cruciform (Fig. 1e, f).

Consider the ON-OFF-DSGC subtype we call 'V-cells', after their preference for ventral motion on the retina, or ventral motion of the mouse ('upward' motion in the visual field; red lobes in Fig. 1m). V-cells preferred motion towards a centre of contraction in the ventral retina, and everywhere paralleled a ventrally directed translatory optic flow field (Fig. 1m, red meridians). We extended this analysis by targeted patch recording of GFP-tagged V-cells in Hb9-GFP mice<sup>21</sup>. They preferred motion towards a ventral singularity (Fig. 2a, black arrows; Extended Data Fig. 2l–r), just as imaged V-cells did (Fig. 1m), aligned everywhere with the same translatory optic flow (Figs 1m and 2a, red meridians). Dendritic-field asymmetries of V-cells, which correlate with preferred direction<sup>21</sup> (Extended Data Fig. 2q), also aligned with this flow field (Fig. 2a, gold arrowheads). Thus, as an ensemble, V-cells respond best to a specific translatory optic flow, produced by roughly downward motion.

Other subtypes of ON-OFF-DSGCs also adhered to translatory optic-flow geometry. In Trhr-GFP mice<sup>15</sup>, we targeted 'N-cells' preferring nasal retinal motion, for recordings. N-cells preferred motion away from a centre of expansion in temporal retina (Fig. 2b), following a distinct translatory flow field (blue meridians). To assess a third subtype, 'T-cells', preferring temporal retinal motion (Fig. 2c), we analysed imaged ON-OFF-DSGCs that were immunonegative for CART (cocaine and amphetamine regulated transcript)<sup>22,23</sup>. T-cell preferences too were aligned with a translatory optic flow field (green meridians), here with a centre of contraction in the temporal retina (Fig. 2c).

To quantify how well the DS preferences of a cell sample align with any single optic flow field, we devised a concordance index—the percentage of cells preferring directions within 10° of local flow. Repeating such template-matching for many possible translatory axes ( $n = 2,701$ ; 5° resolution), we generated a spherical tuning plot, displaying concordance as a function of the axis of translation. Hot spots show directions of translation inducing flow best aligned with observed DS preferences and thus driving maximal net output of this neuronal ensemble (Extended Data Fig. 5a–d; Methods).

Figure 2d shows such a translatory flow-tuning plot for patch-recorded Hb9 V-cells. Longer spikes and warmer map colours indicate better concordance and point to a location in space around the mouse, the centre of flow convergence. To facilitate comparisons, we cartographically flattened these plots (Fig. 2j, k). The flattened plot for V-cells (Fig. 2g) exhibits one hot spot at the visual coordinates of the optimal centre of contraction. So do the other two molecularly defined ON-OFF subtypes (Trhr N-cells; CART-negative T-cells; Fig. 2b, c, e, f, h, i). Each subtype thus has a single best translation. The N- and T-cell hot spots are separated by about 180° in polar direction (abscissa), suggesting that they share a common axis, while the V-cell hot spot (Fig. 2g) is offset 90°, indicating preference for translation along an orthogonal axis (Supplementary Note 3).

The flow-tuning plot for all imaged ON-OFF-DSGCs featured four prominent hot spots separated by about 90° around the margin of the visual field or retina (Fig. 3a–c). Three of them correspond to V-, N-, and T-cell hot spots (Fig. 2d–f), and the last evidently to D-cells, preferring dorsal retinal motion. The best axes of N- and T-cells are effectively aligned, as are those for D- and V-cells (Fig. 3b). Thus ON-OFF-DSGCs comprise two pairs of subtypes, each pair preferring translation along the same axis, but in opposite directions.

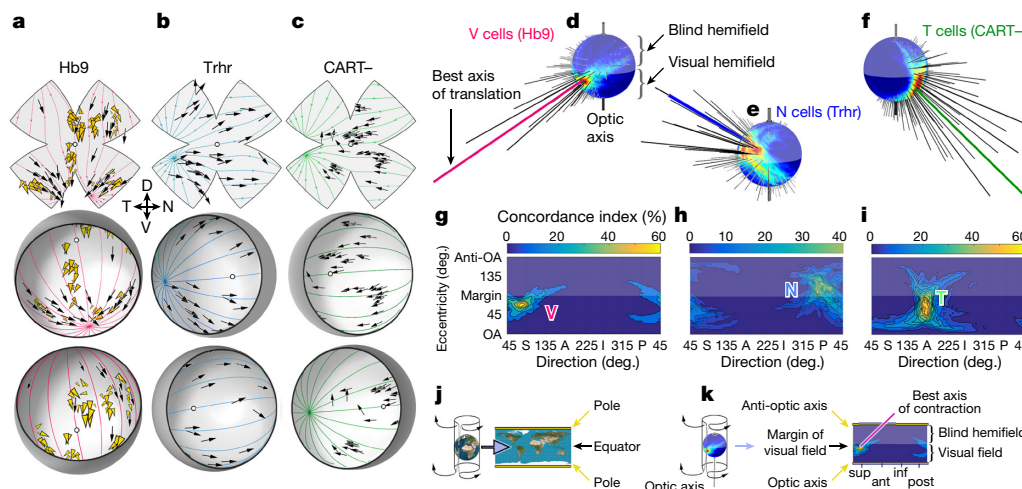


**Figure 2 | Genetically defined ON-OFF-DSGC subtypes align DS preferences with translatory optic flow.** **a–c**, DS preferences of molecularly defined ON-OFF-DSGC subtypes, assessed electrophysiologically (black arrows) and plotted on standard flattened (above) and reconstructed hemispheric retinas viewed from two perspectives (below). **a**, V-cells, preferring ventral motion, targeted in Hb9-GFP mice. Gold arrowheads indicate orientations of dendritic asymmetry. **b**, N-cells, preferring nasal motion, targeted in Trhr-GFP mice. **c**, T-cells, preferring temporal motion, identified by immunonegativity for CART. Coloured lines in **a–c** indicate best-fitting translatory optic flow. **d–k**, Quantitative assessment and cartographic representation of best translatory axes for DSGC ensembles. **d**, Concordance index (goodness of fit) as a function of axis of translation for recorded Hb9 V-cells, plotted as a spherical flow-tuning

map. Optic axis (projection of optic disk into central visual field) points downward in this view. Hot spot and longest spike (red) point to visual-field location of the centre of contraction of the translatory flow field best aligned with the direction preferences of sampled cells. **g**, Cartographically flattened (*plate carré*) projection of the flow-tuning plot in **d**. The spherical (**d**) and flattened plots (**g**) both exhibit the same hot spot near the superior (S) edge of the visual field. Equivalent plots shown for N-cells (**e, h**; **e** is rotated 90° to display hot spot) and T-cells (**f, i**), with optimal optic flow either diverging from (N-cells) or converging at a singularity in the anterior visual field. S, superior; A, anterior; I, inferior; and P, posterior. **j, k**, Schematic explication of cartographic flattening of Earth (**j**) or spherical translatory tuning plots (**k**) by *plate carré* projection. S, superior (sup); A, anterior (ant); I, inferior (inf); and P, posterior (post).

How well does this geometric description predict the DS preferences of DSGCs? We modelled four ON-OFF-DSGC channels adhering to the inferred translatory-flow-matching geometry. Each channel comprised modelled cells with locations matched to imaged DSGCs but with preferences aligned exactly with one of the four cardinal translatory flow fields. Angular jitter (about 10°) was added to mimic biological and experimental variability. As expected, flow-tuning plots for single modelled channels (Fig. 3e–h) exhibited one hot spot (that is, best axis; compare Fig. 2g–i). The approximately 90° intervals between hot spots reflect the orthogonality of the two cardinal axes. Randomizing modelled preferences yielded a plot of uniformly mediocre concordance (Fig. 3i). We differentially weighted each channel to reproduce its apparent abundance in our sample (Extended Data Fig. 5f–j; Methods) and summed them. The flow-tuning plot for the best-fitting model (Fig. 3d) was strikingly similar to that for the real data (Fig. 3c;  $R^2 = 0.97$ ). The fit was optimal when the relative abundance of subtypes was  $N > V > D$  or T (Fig. 3k). Local polar plots of DS preference for modelled cells (Fig. 3j; black) faithfully reproduced those for real cells (gold).

The model also recapitulated the behaviour of other subsets of ON-OFF-DSGCs (Hb9; Trhr; CART-negative or CART-positive; Fig. 3l–p, left); see meridians in Fig. 2a–c. Weighting coefficients (Fig. 3l–p, bar plots) provide estimates of relative abundances of subtypes in each sample; three molecularly defined samples effectively comprised single subtypes (Fig. 3l–o; bar plots).

### ON-DSGCs prefer the same translatory optic flows

ON-DSGCs ostensibly comprise three subtypes preferring directions approximately 120° apart<sup>18,19</sup>, implying a global architecture distinct from that of ON-OFF-DSGCs. We suspected single ON-DSGC ensembles might prefer rotatory optic flow because they innervate the accessory optic system (AOS), which encodes rotatory slip and drives optokinetic image stabilization<sup>24,25</sup>. Surprisingly, ON-DSGCs proved virtually identical in global architecture to ON-OFF-DSGCs (Fig. 4). They, too, comprised four subtypes (N-, T-, D-, and V-type ON-DSGCs). Each subtype aligned its DS preferences everywhere with

essentially the same translatory flow field as its ON-OFF-DSGC counterpart. As before, four lobes approximately 90° apart were discernible in the polar plots of all ON-DSGCs (Fig. 4b) and became more distinct when the central retina was selectively sampled (Fig. 4c).

The unexpected similarity between ON-DSGCs and ON-OFF-DSGCs is not an artefact of misidentification (Supplementary Discussion; Extended Data Figs 1e–l, 3h, 6 and 7i–n). Why, then, do we find four ON-DSGC subtypes instead of three? ON-DSGC N-cells were less common (Fig. 4b, c) and less well-tuned than other ON-DSGC subtypes (Fig. 4e). A stringent direction-selectivity-index (DSI) criterion excluded virtually all of them, resulting in a three-lobed polar plot reminiscent of the classic one (Fig. 4d, Supplementary Note 4).

Like ON-OFF-DSGCs, ON-DSGCs aligned their preferred directions with optic flow produced by translation along one of two mutually orthogonal axes. Each is served by a pair of subtypes, generating paired hot spots at diametrically opposed global locations (Fig. 4i) or separated by 180° in flattened maps (Fig. 4j). Cardinal translatory axes were virtually identical for ON-DSGCs and ON-OFF-DSGCs (Fig. 4i).

An adaptation of the model developed for ON-OFF-DSGCs faithfully recapitulated the flow-tuning plot for ON-DSGCs (Fig. 4j, k;  $R^2 = 0.95$ ) and topographic variations in local DS preference (Fig. 4h). Real and modelled ON-DSGCs consistently matched ON-OFF-DSGCs in DS preference (Fig. 4h). However, the weighting of individual subtypes differed (Fig. 4m); D-cells were the most abundant ON-DSGC subtype. Retrograde tracing revealed that ON-DSGC subtypes project differentially to components of the AOS (Extended Data Figs 2g–k, 3i–m).

### DSGCs encode translatory motion along two key axes

From resting eye and head positions, we determined the orientation of these cardinal translatory axes of DSGCs relative to the visual environment (Methods). The N/T-cell axis approximated the anteroposterior (longitudinal body) axis, whereas the D/V-cell axis corresponded closely to the gravitational axis (Fig. 5a). Because N-cells, as an ensemble, respond best to forward translation along the body axis (ambulation),

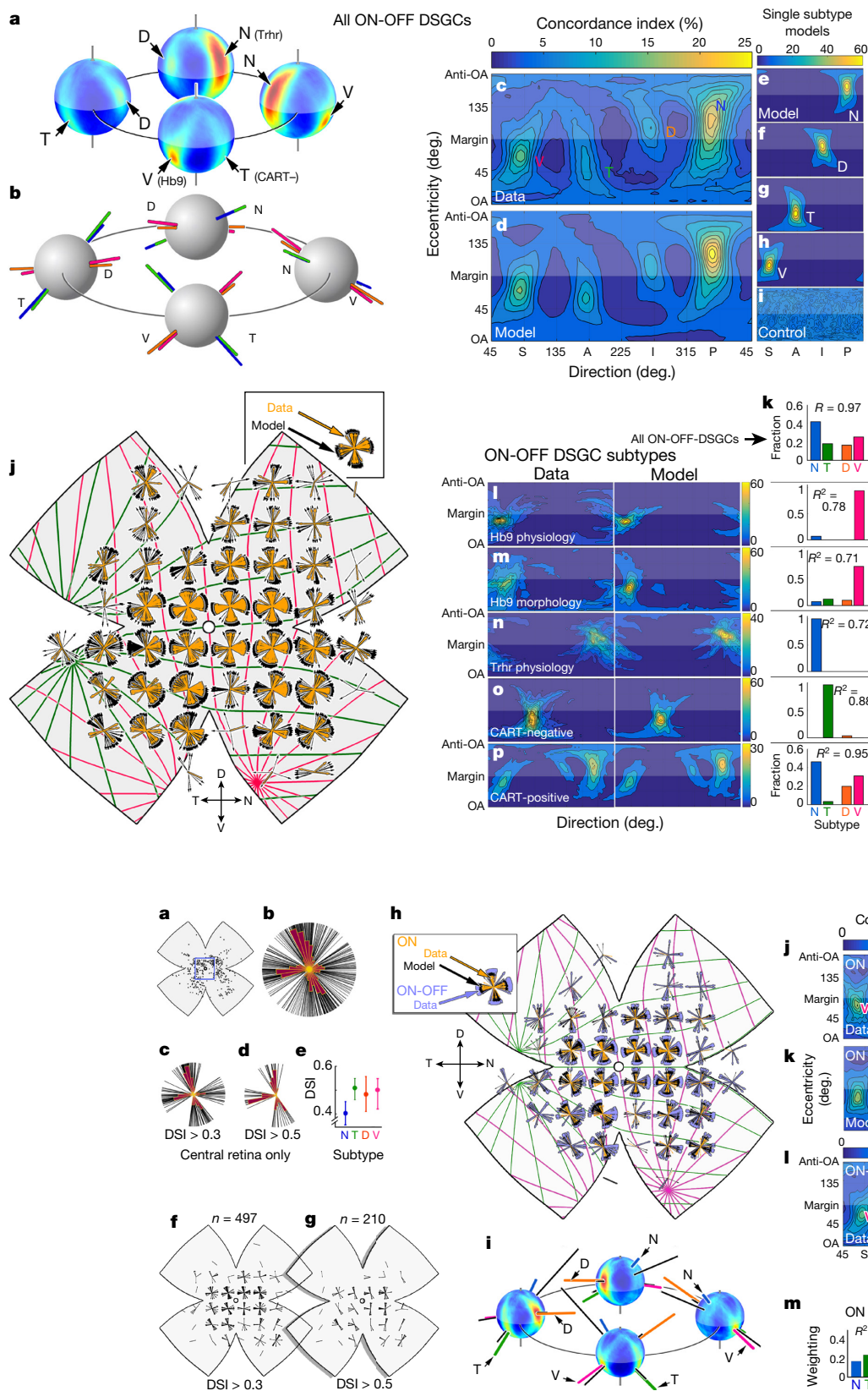


**Figure 3 | Direction preferences of ON-OFF-DSGCs align globally with two axes of translatory optic flow.** **a**, Spherical translatory-flow tuning plot for all ON-OFF-DSGCs, from four perspectives. Four hot spots are apparent, one per subtype (compare Fig. 2d–f). **b**, Best translatory axes are aligned for D- and V-cells (orange; red), and for N- and T-cells (blue; green). **c**, Flattened version of translatory-flow-tuning plot in **a** (compare Fig. 2g–k) is recapitulated by a model (**d–h**) comprising four subtype ensembles (**e–h**), weighted as in **k**, **i**. Control flow-tuning map (randomized DS preferences). See Supplementary Note 3 for clarification. **j**, Local polar plots of DS preference for modelled cells (black) recapitulate the same topographic variations for imaged cells (gold). Coloured meridians plot the two best-fitting translatory optic flows. **l–o**, Left column, flattened flow-tuning maps for effectively pure single-subtype samples. **l, m**, V-cells (Hb9-GFP); **n**, N-cells (Trhr-GFP); **o**, T-cells (CART-immunonegative). **p**, Same, but for all subtypes but T-cells using CART-immunopositivity. Best-fitting models (middle column) reproduce the actual plots; optimal weighting factors (bar plots at right) confirm subtype purity.

**Figure 4 | ON-DSGCs unexpectedly match global geometry of ON-OFF-DSGCs with four channels and four cardinal translatory directions.** Locations **(a)** and DS preferences **(b–d)** of imaged ON-DSGCs. **b**, All cells; **c, d**, central retina (square in **a**). Four subtypes (lobes) are apparent in the central retina (**c**) but N-cells are less well-tuned for direction **(e)**, so N-cell lobe vanishes under a more stringent tuning criterion **(d, f, g)**. **h**, Topography of DS preference among ON-DSGCs (gold) resembles that of ON-OFF-DSGCs (purple) and of modelled ON-DSGCs (black) aligned

with optimal orthogonal translatory optic flow fields (coloured meridians). **i**, Spherical flow-tuning plot for all ON-DSGCs; four perspectives. Best axes for the four subtypes (coloured) form two co-linear pairs defining two perpendicular cardinal translatory axes closely matching those of ON-OFF-DSGCs (black). **j–m**, Flow tuning plot for all ON-DSGCs (**j**) reveals four channels well described by the model (**k**) and closely resembling the equivalent plot for imaged ON-OFF-DSGCs (**l**) (from Fig. 3c) except for the relative weighting of channels (**m**).

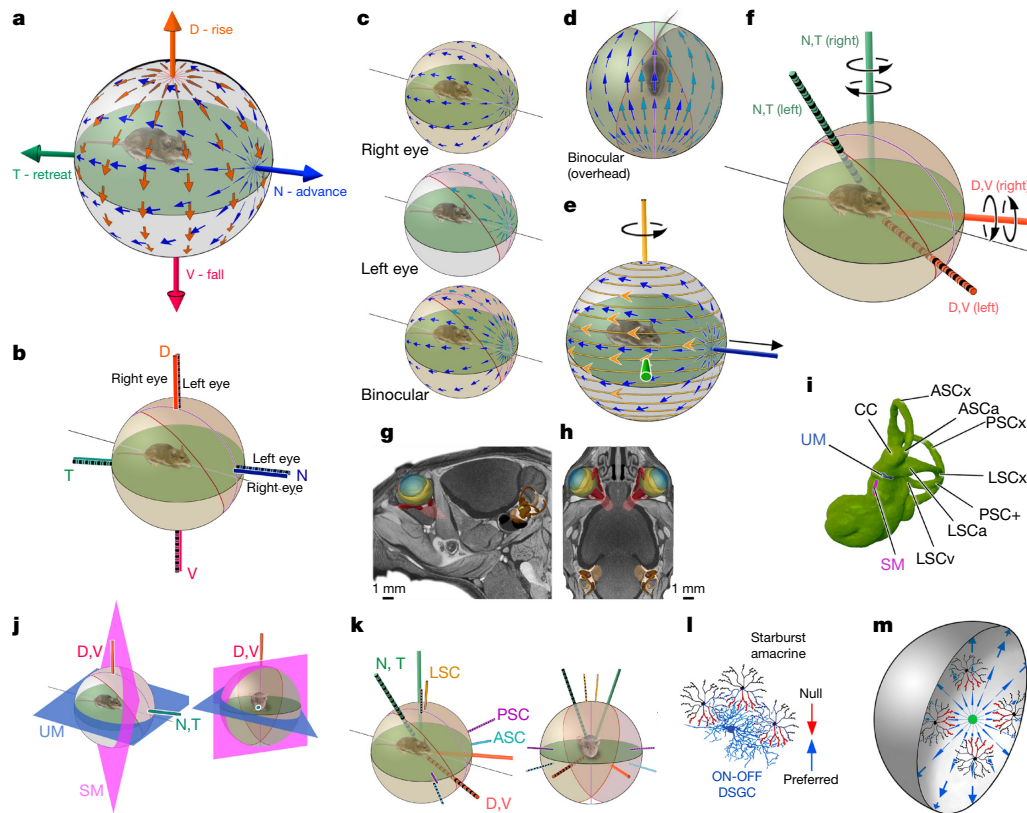


**Figure 5 | Global geometry of retinal DS ensembles permits coding of translatory and rotatory self-motion.** **a**, Orientation of best translatory axes in space around the mouse, roughly midaxial and gravitational. **b**, Orientation of best translatory axes is identical for both eyes; thus a single translatory optic flow optimally activates the N-cell ensemble in both the right and left eyes (**c**, **d**). **e**, Geometric basis of sensitivity of DS ensembles to rotatory optic flow. In central retina, ‘advance’ or N-cells (blue arrows) align their preferences with optic flow (gold lines and arrowheads) produced by rotation around a vertical axis (gold) orthogonal to their best translatory axis (blue). **f**, Best rotatory axes of N- and T-cells (green) and V- and D-cells (orange) in the two eyes; left-eye axes

striped. **g–i**, Micro computed tomography (microCT) reconstruction of vestibular system in context from side (**g**), above (**h**), or in isolation (**i**). See Supplementary Note 7 for abbreviations. **j**, Relationship of cardinal DSGC translatory axes to otolith planes. **k**, Relationship of best rotatory axes of DSGCs (thick) to those of semicircular canals (thin); axes for left eye and labyrinth are striped. **l**, Asymmetric starburst amacrine cell wiring underlying retinal DS. Each DSGC responds to motion in the preferred direction but not in the opposite (null) direction. **m**, Current findings imply wiring asymmetries for a given DS subtype (blue) vary topographically and are oriented towards or away from a singularity.

it is appropriate to call them ‘advance cells’. By extension, T-, V-, and D-cells are ‘retreat’, ‘fall’, and ‘rise’ cells. The cardinal translatory axes are virtually identical for the two eyes (Fig. 5b), so members of one subtype prefer the same global flow regardless of their location in either retina. Together, they form a binocular, near-panoramic cell array responding best to a specific translatory optic flow field and thus to self-motion in a cardinal direction (Fig. 5c, d).

### Retinal DSGCs also encode rotatory optic flow

It is surprising that ON-DSGCs adhere to translatory optic-flow geometry because they supply directional information to the AOS and flocculus, which encode rotatory flow<sup>25</sup>. However, an ensemble aligned with translatory optic flow (Fig. 5e, blue) will also respond differentially to rotatory optic flow (Fig. 5e–f; Extended Data Fig. 8o–s; Supplementary Note 5). Might DSGC ensembles actually adhere to a rotatory flow geometry and, only secondarily, exhibit tuning for translation? Apparently not. The translatory model significantly outperformed the best rotatory one for every sample tested, including all imaged ON-OFF-DSGCs ( $R^2 = 0.97$  versus 0.92) and ON-DSGCs ( $R^2 = 0.95$  versus 0.87) (Supplementary Note 6; Extended Data Fig. 8a–n).

### Relative activity of subtypes encodes self-motion

Thus, a single DSGC ensemble’s pooled output provides ambiguous information about self-motion. However, the brain could distinguish

translation from rotation by comparing the relative activation of DS-subtype ensembles in the two eyes. For example, forward translation activates the same subtype (N-cells) in both eyes, whereas leftward rotation activates opposing subtypes (right eye, N; left eye, T). More generally, every possible translatory or rotatory optic flow produces a unique pattern of activation across the eight DS channels (2 axes  $\times$  2 directions  $\times$  2 eyes; Extended Data Fig. 9a–e). Indeed, a simple decoder using only relative activation of channels can distinguish translation from rotation and infer the motion axis (Extended Data Fig. 9f, g). Similarly, modelled postsynaptic cells differentially tuned for rotation or translation were easily constructed by summing or subtracting specific subtype signals from the two eyes (Extended Data Fig. 10).

### Relationship between visual and vestibular channels

We have shown how retinal DS channels decompose reafferent visual motion signals into translatory (otolith-like) and rotatory (canal-like) components. Tomographic reconstruction revealed that cardinal vestibular axes and planes lie near, but do not precisely match, their DSGC analogues (Fig. 5g–k; Supplementary Methods; Supplementary Notes 7, 8).

### Discussion

All canonical DSGCs organize their directional preferences around the geometry of optic flow produced by translatory self-motion along two axes of high behavioural relevance: the body axis and the gravi-

tational axis. They comprise 16 channels altogether: 4 cardinal directions of translation encoded per eye  $\times$  2 eyes  $\times$  2 DSGC classes (ON and ON-OFF). Subtype ensembles also respond differentially to rotatory optic flow. Any arbitrary translation or rotation will activate these 16 channels in a unique pattern that the brain presumably decomposes into translatory and rotatory components. A table summarizing the properties of DSGC subtypes, their preferred translations and rotations, and their relation to previously reported DSGC subtypes and reporter mice is provided (Supplementary Table 1).

Eye movements in freely moving rodents appear driven largely by the vestibulo-ocular reflex<sup>26</sup> and optokinetic nystagmus, which compensate for head movements to stabilize the retinal image. The alignment between visual and vestibular axes, imperfect even at rest (Fig. 5j, k), would be further degraded by such deviations of the eye. The brain presumably compensates when coupling these two reafferent streams to common motor outputs. On the other hand, because vestibulo-ocular reflex and optokinetic nystagmus are image-stabilizing eye movements, they defend the alignment between DSGC cardinal translatory axes and the gravitational and body axes when the head rotates<sup>26</sup>. Gaze shifts transiently reorient the cardinal translatory directions in space around the mouse, but eye and head typically return promptly to primary position<sup>26</sup>, re-establishing the alignment of cardinal visual directions with gravitational and body axes.

The matching of DS geometry to translatory optic flow may reflect the earlier evolutionary origins of translation-sensitive, as compared to rotation-sensitive, vestibular organs<sup>27</sup>. Retinotopic information from DS ensembles is preserved in mappings to the colliculus and geniculocortical system<sup>13</sup>, permitting higher-order computations based on retinal motion.

Anatomical asymmetries of starburst-amacrine-cell inhibition generate direction preference in DSGCs<sup>8</sup>. Our data imply that these asymmetries are the same for ON-DSGCs and ON-OFF-DSGCs, and are organized around two retinal singularities, corresponding to the centres of expansion or contraction of cardinal translatory flow fields (Fig. 5l, m).

**Online Content** Methods, along with any additional Extended Data display items and Source Data, are available in the online version of the paper; references unique to these sections appear only in the online paper.

**Received 27 May 2016; accepted 16 May 2017.**

**Published online 7 June 2017.**

1. Vaney, D. I., He, S., Taylor, W. R. & Levick, W. R. In *Motion Vision — Computational, Neural, and Ecological Constraints* (eds Zanker, J. M. & Zeil, J.) 13–56 (Springer, 2001).
2. Wei, W., Hamby, A. M., Zhou, K. & Feller, M. B. Development of asymmetric inhibition underlying direction selectivity in the retina. *Nature* **469**, 402–406 (2011).
3. Taylor, W. R., He, S., Levick, W. R. & Vaney, D. I. Dendritic computation of direction selectivity by retinal ganglion cells. *Science* **289**, 2347–2350 (2000).
4. Oesch, N., Euler, T. & Taylor, W. R. Direction-selective dendritic action potentials in rabbit retina. *Neuron* **47**, 739–750 (2005).
5. Demb, J. B. Cellular mechanisms for direction selectivity in the retina. *Neuron* **55**, 179–186 (2007).
6. Ding, H., Smith, R. G., Poleg-Polsky, A., Diamond, J. S. & Briggman, K. L. Species-specific wiring for direction selectivity in the mammalian retina. *Nature* **535**, 105–110 (2016).
7. Kim, J. S. *et al.* Space-time wiring specificity supports direction selectivity in the retina. *Nature* **509**, 331–336 (2014).
8. Briggman, K. L., Helmstaedter, M. & Denk, W. Wiring specificity in the direction-selectivity circuit of the retina. *Nature* **471**, 183–188 (2011).
9. Park, S. J., Kim, I. J., Looger, L. L., Demb, J. B. & Borghuis, B. G. Excitatory synaptic inputs to mouse on-off direction-selective retinal ganglion cells lack direction tuning. *J. Neurosci.* **34**, 3976–3981 (2014).
10. Angelaki, D. E. & Hess, B. J. Self-motion-induced eye movements: effects on visual acuity and navigation. *Nat. Rev. Neurosci.* **6**, 966–976 (2005).
11. Angelaki, D. E. & Cullen, K. E. Vestibular system: the many facets of a multimodal sense. *Annu. Rev. Neurosci.* **31**, 125–150 (2008).

12. Yang, G. & Masland, R. H. Receptive fields and dendritic structure of directionally selective retinal ganglion cells. *J. Neurosci.* **14**, 5267–5280 (1994).
13. Cruz-Martín, A. *et al.* A dedicated circuit links direction-selective retinal ganglion cells to the primary visual cortex. *Nature* **507**, 358–361 (2014).
14. Huberman, A. D. *et al.* Genetic identification of an on-off direction-selective retinal ganglion cell subtype reveals a layer-specific subcortical map of posterior motion. *Neuron* **62**, 327–334 (2009).
15. Rivlin-Etzion, M. *et al.* Transgenic mice reveal unexpected diversity of on-off direction-selective retinal ganglion cell subtypes and brain structures involved in motion processing. *J. Neurosci.* **31**, 8760–8769 (2011).
16. Chan, Y. C. & Chiao, C. C. The distribution of the preferred directions of the ON-OFF direction selective ganglion cells in the rabbit retina requires refinement after eye opening. *Physiol. Rep.* **1**, e00013 (2013).
17. Oyster, C. W. Analysis of image motion by rabbit retina. *J. Physiol. (Lond.)* **199**, 613–635 (1968).
18. Oyster, C. W. & Barlow, H. B. Direction-selective units in rabbit retina: distribution of preferred directions. *Science* **155**, 841–842 (1967).
19. Kanjhan, R. & Sivyer, B. Two types of ON direction-selective ganglion cells in rabbit retina. *Neurosci. Lett.* **483**, 105–109 (2010).
20. Kwong, J. M. K., Quan, A., Kyung, H., Piri, N. & Caprioli, J. Quantitative analysis of retinal ganglion cell survival with Rbpms immunolabeling in animal models of optic neuropathies. *Invest. Ophthalmol. Vis. Sci.* **52**, 9694–9702 (2011).
21. Trenholm, S., Johnson, K., Li, X., Smith, R. G. & Awatramani, G. B. Parallel mechanisms encode direction in the retina. *Neuron* **71**, 683–694 (2011).
22. Dhande, O. S. *et al.* Genetic dissection of retinal inputs to brainstem nuclei controlling image stabilization. *J. Neurosci.* **33**, 17797–17813 (2013).
23. Kay, J. N. *et al.* Retinal ganglion cells with distinct directional preferences differ in molecular identity, structure, and central projections. *J. Neurosci.* **31**, 7753–7762 (2011).
24. Simpson, J. I., Leonard, C. S. & Soodak, R. E. The accessory optic system of rabbit II. Spatial organization of direction selectivity. *J. Neurophysiol.* **60**, 2055–2072 (1988).
25. Simpson, J. I., Leonard, C. S. & Soodak, R. E. The accessory optic system — analyzer of self motion. *Ann. NY Acad. Sci.* **545**, 170–179 (1988).
26. Wallace, D. J. *et al.* Rats maintain an overhead binocular field at the expense of constant fusion. *Nature* **498**, 65–69 (2013).
27. Nilsson, D. E. The evolution of eyes and visually guided behaviour. *Phil. Trans. R. Soc. Lond. B* **364**, 2833–2847 (2009).

**Supplementary Information** is available in the online version of the paper.

**Acknowledgements** We thank J. Demb and W. Wei for providing us with Trhr-GFP and Drd4-GFP mice. Countless colleagues provided theoretical, data-analytic and technical advice, including imaging, electronics and device synchronization, intracranial and intraocular injections, electrophysiological recordings and statistical analysis. They included J. McLwain, B. Borghuis, G. Williams, C. Deister, J. Voigts, C. Moore, D. Sheinberg, K. Briggman, M. Fogerson, M. E. Stabio, J. Renna, S. Cruikshank, S. Crandall, B. Connors, S. Guan, J. Sanes, W. Truccolo and C. Aizenman. D. Boghossian maintained the mouse colony and genotyped experimental mice. K. Boghossian, C. Papendrop and P.-N. Chiang contributed to digital image analysis. J. Murphy constructed microscope stages and retinal mounts. We thank V. Jayaraman, D. S. Kim, L. L. Looger and K. Svoboda from the GENIE Project, Janelia Research Campus, Howard Hughes Medical Institute for sharing their GCaMP6f calcium indicator. This project was supported by the Banting Postdoctoral Fellowship of Canada (S.S.), The Sidney A. Fox and Dorothea Doctors Fox Postdoctoral Fellowship in Ophthalmology and Visual Sciences (S.S.), NSF-RTG grant DMS-1148284 (J.A.G.), and NIH grant R01 EY12793 and an Alcon Research Institute Award (D.M.B.).

**Author Contributions** D.M.B. and S.S. designed the study and developed the theoretical framework. S.S. performed all imaging, electrophysiological recordings and intracellular dye-fills. S.S., A.B.L., G.M., G.C. and J.K.S. performed intracranial and intraocular injections, immunostaining of retinas and brains, and calcium imaging data processing. J.A.G. developed the mathematical methods for interconverting locations on flattened retinas to hemispherical ones and to global space around the mouse. N.J. performed the tomographic analysis of the vestibular system. S.S., D.M.B., J.A.G. and N.J. analysed the data. D.M.B., S.S., J.A.G. and N.J. wrote the paper.

**Author Information** Reprints and permissions information is available at [www.nature.com/reprints](http://www.nature.com/reprints). The authors declare no competing financial interests. Readers are welcome to comment on the online version of the paper. Publisher's note: Springer Nature remains neutral with regard to jurisdictional claims in published maps and institutional affiliations. Correspondence and requests for materials should be addressed to D.M.B. ([david\\_berson@brown.edu](mailto:david_berson@brown.edu)) or S.S. ([shai\\_sabbah@brown.edu](mailto:shai_sabbah@brown.edu)).

**Reviewer Information** *Nature* thanks J. Demb, A. Rosenberg, J. R. Sanes and the other anonymous reviewer(s) for their contribution to the peer review of this work.

## METHODS

**Sample size.** No statistical methods were used to predetermine sample size.

**Randomization and blinding.** Unless otherwise stated, the experiments were not randomized and the investigators were not blinded to allocation during experiments and outcome assessment.

**Animals.** All procedures were in accordance with National Institutes of Health guidelines and approved by the Institutional Animal Care and Use Committee at Brown University. We used three strains of adult mice of either sex, 2–2.5 months old: wildtype C57BL/6J (Jackson Laboratory), or Hb9-GFP (B6.Cg-Tg(Hlx9-GFP)1Tmj/J; Jackson Laboratory) or Trhr-GFP (Tg(Trhr-EGFP)HU193Gsat; MMRR) reporter mice.

**Intravitreal injections of calcium indicator.** Mice (C57BL/6J) were anaesthetized with isoflurane (3% in oxygen; MatrX VIP 3000, Midmark). A viral vector inducing expression of the calcium indicator GCaMP6f (AAV2/1.hSynapsin.GCaMP6f; Vector Core, UPenn; 1.5–2  $\mu$ l of  $\sim 3 \times 10^{13}$  units ml<sup>-1</sup>) was injected into the vitreous humour of the right eye through a glass pipette using a microinjector (Picospritzer III, Science Products GmbH). Animals were killed and retinas harvested 14–21 d later. GCaMP6f was expressed mainly in RGCs and amacrine cells of the ganglion-cell layer, most densely near central retinal blood vessels.

**Retrograde labelling.** Mice were anaesthetized as for eye injections and secured in a stereotaxic apparatus. Respiration and body temperature were monitored. A micropipette (1B100-4, World Precision Instruments) filled with a retrograde tracer (1  $\mu$ l; cholera toxin beta-subunit conjugated to CF568; CTB-568; 1  $\mu$ g  $\mu$ l<sup>-1</sup> PBS; Biotium #00071) was positioned stereotaxically. Tracer was injected pneumatically (Picospritzer; Parker Hannifin; 10 PSI; 400 ms pulses) and the pipette slowly withdrawn after 10 min. The wound was sutured and the mouse monitored until able to remain upright. Analgesia (Buprenex SR, subcutaneous) minimized postoperative pain.

**Tissue harvest and retinal dissection.** The right eye was removed and immersed in oxygenated Ames medium (95% O<sub>2</sub>, 5% CO<sub>2</sub>; Sigma-Aldrich; supplemented with 23 mM NaHCO<sub>3</sub> and 10 mM D-glucose). In retrograde-labelling experiments, the brain was also removed and fixed by immersion in 4% paraformaldehyde overnight. Under dim red light, the globe was cut along the ora serrata, and cornea, lens and vitreous humour removed. Four radial relieving cuts were made in the eyecup, the largest centred on the insertions of the lateral and medial recti, useful later as a reference axis. The other two were deliberately asymmetric (roughly dorso-temporal and ventral) to disambiguate retinal orientation. The retina was flat-mounted on a custom-machined hydrophilic polytetrafluoroethylene membrane (cell culture inserts, Millicell<sup>28</sup>) using gentle suction, and secured in a chamber on the microscope stage. Retinas were continuously superfused with oxygenated Ames' medium (32–34 °C). The left eye was enucleated and photographed for measurement of arc length from optic disk to ora serrata, a parameter needed for mapping flat-mounted retina data to spherical coordinates (see Extended Data Fig. 4 and Supplementary Equations).

**Immunohistochemistry of retina and brain.** After imaging or recording, retinas were fixed (4% paraformaldehyde, 30 min, 20 °C) and counterstained with one or more antibodies: (1) rabbit anti-CART (cocaine and amphetamine regulated transcript; H00362, Phoenix Pharmaceuticals)—a specific marker for most ON-OFF DSGCs<sup>23</sup>; (2) guinea pig anti-RBPMS (RNA-binding protein with multiple splicing; 1832-RBPMS, PhosphoSolutions), a pan-ganglion-cell marker<sup>20</sup>; or (3) chicken anti-GFP (Abcam), to enhance the fluorescence of the GFP-based GCaMP6f indicator, which helped us to align images captured during live imaging with subsequent histology. Using a custom-designed rotating stage, we oriented the processed retina in the multiphoton microscope to match that during calcium imaging, then acquired confocal one-photon Z-stacks of all fluorophores (including retrograde tracers) in the RGC layer. Brains were embedded in 4% agarose, cut coronally (50  $\mu$ m) on a vibrating microtome and immunostained using rabbit anti-GFP (Life Technologies, A-11122) to enhance GCaMP6f fluorescence in retinal axons, useful for localizing deposits in relation to fasciculi and terminal nuclei of the AOS.

**Patch recording and dye filling of ganglion cells.** Whole-cell patch-clamp recordings of isolated flat-mount retinas were performed under current-clamp using a Multiclamp 700B amplifier, Digidata 1550 digitizer, and pClamp 10.5 data acquisition software (Molecular Devices; 10 kHz sampling). Pipettes were pulled from thick-walled borosilicate tubing (P-97, Sutter Instruments). Tip resistances were 4–8 M $\Omega$  when filled with internal solution, which contained (in mM): 120 K-gluconate, 5 NaCl, 4 KCl, 2 EGTA, 10 HEPES, 4 ATP-Mg, 7 phosphocreatine-Tris, and 0.3 GTP-Tris, pH 7.3, 270–280 mOsm). We added red fluorescent dye (Alexa Fluor 568, Invitrogen) for visual guidance during two-photon imaging and intracellular dye-filling.

Selected calcium-imaged cells were dye-filled (Alexa Fluor 568 hydrazide, Invitrogen) using fine glass pipettes ( $\sim 50$  M $\Omega$  resistance) guided by two-photon imaging. A current pulse (–20 nA, 100 ms) triggered cell penetration. Dye was

iontophoretically injected (20–60 biphasic current pulses; –2,000 pA for 500 ms and +500 pA for 400 ms) until dendrites were well filled. After all calcium imaging was completed, filled cells were documented in Z-stacks acquired in confocal (single-photon) mode.

**Two-photon functional imaging.** Imaging was conducted on an Olympus FV1200MPE BASIC (BX-61WI) microscope equipped with a 25 $\times$ , 1.05 NA water-immersion objective (XLPL25XWMP, Olympus) and an ultrafast pulsed laser (Mai Tai DeepSee HP, Spectra-Physics) tuned to 910 nm. Epifluorescence emission was separated into 'green' and 'red' channels with a 570 nm dichroic mirror and a 525/50 bandpass filter (FF03-525/50-32, Semrock, green channel) and 575–630 nm bandpass filter (BA575-630, Olympus, red channel), respectively. The microscope system was controlled by FluoView software (FV10-ASW v.4.1). Images of 256  $\times$  128 pixels representing 256  $\times$  128  $\mu$ m on the retina were acquired at 15 Hz (zoom setting of 2).

**Visual stimulation.** Patterned visual stimuli, synthesized by custom software using Psychophysics Toolbox under Matlab (The MathWorks), were projected (AX325AA, HP) and focused onto photoreceptor outer segments through the microscope's condenser. The projected display covered 1.5  $\times$  1.5 mm; each pixel was 5  $\times$  5  $\mu$ m. The video projector was modified to use a single UV LED lamp (NC4U134A, Nichia). The LED's peak wavelength (385 nm) shifted to 395 nm after transmission through a 440 nm short-pass dichroic filter (FF01-440/SP, Semrock), a dichroic mirror (T425lpxr, Chroma), and various reflective neutral density filters (Edmund Optics). Photoisomerization rates were derived from the stimulus spectrum (measured using an absolute-irradiance-calibrated spectrometer; USB4000-UV-VIS-ES, Ocean Optics), estimated rod (0.85  $\mu$ m<sup>2</sup>) and cone (1  $\mu$ m<sup>2</sup>) collecting areas<sup>29</sup>; and spectral absorbances of mouse rod and cone pigments<sup>30</sup>. Rates were very similar among rods and cones ( $\sim 10^4$  R\* photoisomerizations s<sup>-1</sup>), independent of their relative expression of S- and M-cone pigments<sup>31</sup>.

To probe ON and OFF responses, we used a bright bar on a dark background (bar width = 1,500  $\mu$ m, inter-stimulus duration = 5 s) drifting perpendicular to the bar's long axis in 8 randomized directions (45° interval, speed = 300  $\mu$ m s<sup>-1</sup>, 4 repetitions). To assess directional tuning, we used a sinusoidal grating spanning two spatial periods (spatial frequency = 0.132 cycle per degree, Michelson contrast = 0.95, stimulus duration = 3.65 s, inter-stimulus duration = 5 s at uniform mean grating luminance) drifted in 8 randomized directions (45° interval, drift speed = 4.5° s<sup>-1</sup>, 4 repetitions). Grating and bar parameters were optimized for ON-DSGCs<sup>22</sup>. Frames of the stimulus movie appeared for 50  $\mu$ s during the short 185  $\mu$ s interval between successive sweeps of the imaging laser; thus, no stimulus was presented during the interval of laser scanning and associated imaging (300  $\mu$ s per sweep). The very rapid flickering of the visual stimulus (>2,000 Hz) was well above critical fusion frequency in mice<sup>32</sup>.

**ROI selection and data analysis.** Somatic Ca<sup>2+</sup> responses were analysed using FluoAnalyzer<sup>33</sup> and custom Matlab scripts. In each imaged field, we manually defined many regions of interest (ROIs; >500 pixels each); each ROI consisted of one soma expressing enough GCaMP6f to support functional imaging. The space-averaged pixel intensity within such ROIs was the activity readout for the associated cell, a proxy for its spike rate<sup>34</sup>. Fluorescence responses are reported as normalized increases as follows:

$$\frac{\Delta F}{F} = \frac{F - F_0}{F_0} \quad (1)$$

where  $F$  denotes the instantaneous fluorescence and  $F_0$  the mean fluorescence over a 1-s period immediately preceding stimulus onset.

The preferred direction (PD) of a cell was estimated as the angle of the vector sum following<sup>35</sup>:

$$PD = \arg \sum_{\varphi} r(\varphi) e^{i\varphi} \quad (2)$$

where  $r$  is the response amplitude to stimuli moving at direction  $\varphi$  (0°, 45°, ..., 315°). The direction selectivity index (DSI) of cells which may range between 0 (no direction selectivity) and 1 (highest direction selectivity) was calculated as:

$$DSI = \left| \frac{\sum_{\varphi} r(\varphi) e^{i\varphi}}{\sum_{\varphi} r(\varphi)} \right| \quad (3)$$

The response amplitude  $r$  represented the average calcium response from the stimulus onset to 2 s following the termination of the stimulus, to capture the OFF responses and to account for the slow decay time of the calcium response<sup>36</sup>.

**Unsupervised clustering and the diversity of DSGCs.** For decades, seven canonical subtypes of DSGCs have been recognized: three ON-DSGCs and four ON-OFF-DSGCs. Recently, however, several new DSGC types or subtypes have been identified or suggested, including previously unknown OFF-DSGC

types and novel forms of ON-DSGCs and ON-OFF DSGCs (Supplementary Discussion).

To assess how many subtypes might be differentiable in our sample based on calcium-response kinetics, we performed unsupervised clustering using Gaussian Mixture Models. From each cell's response to bar motion in the optimal tested direction, we extracted two features. The first was a response-latency measure. We estimated when the leading edge of the stimulus would first arrive at the receptive-field (assuming a diameter of 300  $\mu\text{m}$  and accounting for cell position within the imaged field), then measured the subsequent delay to the peak of the ON response. The second feature extracted was the slope of the decay during the first 300 ms following the ON peak. For clustering, we used the full covariance matrix, regularized by the addition of a constant (0.001) to guarantee that the estimated covariance matrix is positive. To avoid local minima, we repeated the algorithm using 50 different sets of initial values, with the accepted fit being that with the largest log likelihood. The optimal model (the model with the optimal number of clusters), was estimated based on the Bayesian information criterion:

$$\text{BIC} = -2\log(L) + k\log(n) \quad (4)$$

where  $L$  represents the maximum of the likelihood function of the model,  $k$  represents the number of clusters in the model (0–10 clusters), and  $n$  stands for the number of observations. The model with the lowest BIC was considered optimal, and any model with a BIC no higher than 6 than the optimal was considered an acceptable alternative<sup>37</sup>. Running the clustering routine on all DSGCs ( $n=2,446$ ) yielded an optimal model with six clusters, and a seven-cluster model that was essentially as good. An alternative approach, the Akaike information criterion (AIC), yielded an optimal model with eight clusters and acceptable alternatives with three, four, and seven clusters. Altogether, this analysis provides evidence for 3–8 DSGC clusters, dependent on criteria selected. The relationship between these clusters and known or proposed DSGC subtypes is difficult to work out, though the canonical types are certainly among them, and the novel OFF-DGSCs are not (see Supplementary Discussion). In this Article we therefore fall back on the classical and widely used binary division of DSGCs into ON-DSGC and ON-OFF-DSGC classes. Of course, both classes comprise multiple subtypes. Our findings indicate the presence of at least eight subtypes in total (ON versus ON-OFF classes; four subtypes each, distinguishable by their topographically dependent direction preferences), in good agreement with the BIC and AIC analysis above. Because our analysis considered a limited set of potentially distinguishing parameters, it does not preclude further subdivision of DSGCs.

**Inferring the generic directional tuning curve for DSGCs.** To generate the generic directional tuning function for DSGCs (Extended Data Fig. 9a), we expressed the directional preferences of 56 ON-DSGCs and 141 ON-OFF-DSGCs in terms of normalized spike output as a function of stimulus direction relative to the optimal (determined as described earlier). Each of these tuning curves was fitted with a von Mises distribution<sup>38</sup>:

$$r = r_{\max} e^{\left( \frac{k \cos(\varphi - \frac{\pi}{180})}{e^k} \right)} \quad (5)$$

where  $r_{\max}$  is the peak amplitude,  $k$  is the width of the distribution,  $r$  is the calcium response amplitude to stimuli moving in angle  $\varphi$  ( $0^\circ, 45^\circ, \dots, 315^\circ$ ) away from the preferred direction. The bandwidths of ON-DSGC tuning curves, assessed as full-width at half-maximum (FWHM), did not differ significantly from those of ON-OFF-DSGCs (Welch  $t$ -test for unequal variances,  $t = -1.65$ , d.f. = 86.2,  $P = 0.101$  (two-tailed); average  $\pm$  s.d.,  $131^\circ \pm 16^\circ$  for ON DSGCs and  $135^\circ \pm 13^\circ$  for ON-OFF-DSGCs). Therefore, we estimated the directional tuning of DSGCs, regardless of class and subtype, by averaging the normalized tuning curves of all imaged DSGCs (Extended Data Fig. 9a). The bandwidth of this function (FWHM) was  $135^\circ \pm 14^\circ$ .

**Registration of calcium imaging data.** Initially, retinas were oriented relative to the line connecting nasal and temporal relieving cuts made through rectus muscle insertions. We made a post hoc adjustment to this orientation by exploiting the stereotyped form across retinas of flow-tuning maps for ON-OFF-DSGCs (four 'hot' bands, roughly  $90^\circ$  apart along the direction axis—abscissa; see Extended Data Fig. 5). We assumed that the slight variation in the exact position (direction) of these bands resulted from experimental error in orienting the retina, though we cannot exclude contributions from biological variability. To correct for this presumed rotatory error, we measured the displacement of each retina's flow-tuning map from a reference map of the same form. The reference map was generated by averaging four flow tuning maps in which the hot bands were clear and appeared in similar positions (Extended Data Fig. 5e). For each retina ( $n=26$ ), the rotatory error was taken to be the phase offset of its flow-tuning plot from this standard, determined by convolving the two along a single dimension (direction; abscissa) at a resolution of  $5^\circ$ . The correction factor was the phase shift maximizing

the total amount of energy (brightness) in the convolution matrix. Computationally correcting these rotatory errors registered all retinal data sets, allowing us to pool directional data across retinas. Such offsets had a median value of  $2.5^\circ \pm 11.5^\circ$  (s.d.). We corrected for these when transforming retinotopic data to global coordinates. **Estimating the relative abundance of single subtypes in samples of DSGCs.** For ON-DSGCs and ON-OFF-DSGCs independently, we generated a model comprising four DS subtypes (Fig. 3e–h), each of which aligned its DS preferences everywhere with the optic flow produced by translation along a single, empirically determined best axis (Fig. 3b). Coordinates of these four best axes were derived from the four local maxima (hot spots) in flow-tuning plots. We asked what weighting of these subtypes could best reproduce the translatory-flow-tuning plot for all DSGCs (Fig. 3c, d). Formally, the best fitting flow-tuning map for modelled cells ( $M_f$ ) was derived from the weighted sum of four ( $i = 1, 2, \dots, 4$ ) single-subtype maps  $M_i$  (Fig. 3e–h):

$$M_f = \sum_{i=1}^4 C_i M_i \quad (6)$$

where  $C_i$  denotes the weighting allocated to individual subtype maps. We used least-squares fitting (regress function in Matlab) and the coefficient of determination ( $R^2$ ) for regression models without a constant term<sup>39</sup> to assess the goodness of fit. Two-tailed 95% confidence intervals for  $R^2$  values were calculated using bootstrapping, resampling DS cells with replacement (Supplementary Note 6). **Transforming retinal coordinates into global mouse-centred coordinates.** The retinocentric coordinate system we used was monocular, had its origin at the nodal point of the eye, and specified retinal or visual-field location by two coordinates: eccentricity and direction (Extended Data Fig. 5). 'Eccentricity' was defined as the visual angle between the point of interest and the optic axis (the projection of the optic disk). Eccentricity is  $0^\circ$  at the blind spot and  $90^\circ$  at the margin of the visual hemifield, corresponding to the retinal margin. Eccentricities of  $90^\circ$ – $180^\circ$  correspond to spatial locations outside the visual hemifield. 'Direction' refers to the direction of displacement of the point of interest from the optic axis, where nasal =  $0^\circ$ , dorsal =  $90^\circ$ , temporal =  $180^\circ$  and ventral =  $270^\circ$ .

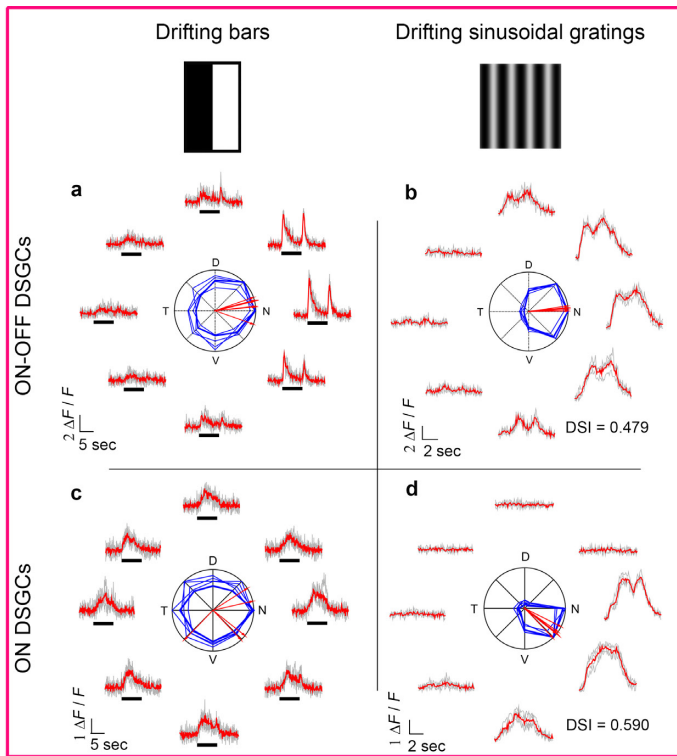
For representations of global visual space, the origin was considered to lie at a point halfway between the two eyes (we neglected the small displacement of the eyes from the midline) (Extended Data Fig. 9). The horizontal plane (elevation =  $0^\circ$ ) was defined as the plane perpendicular to the gravitational axis that passes through the nodal points of the eyes. To translate retinocentric spatial locations to global ones, we assumed that the mouse's head was in a typical ambulatory position<sup>40</sup> which puts the lambda–bregma axis of the skull at an angle of  $29^\circ$  (bregma lower) relative to the anteroposterior axis. Locations in global space were defined by two coordinates: azimuth and elevation. Azimuth corresponds to the angle between a vector pointing straight ahead and a second vector defined by the intersection of two planes: the horizontal, and a vertical plane passing through the eye and the point of interest (azimuth =  $0^\circ$  at the vertical meridian of the visual field). At the horizon, azimuth =  $90^\circ$  lies directly to the right,  $-90^\circ$  lies directly to the left, and  $180^\circ$  lies directly behind the animal. Iso-elevation lines follow lines of latitude in the same global coordinate system, and range from  $90^\circ$  at the zenith, through  $0^\circ$  at the horizontal plane, to  $-90^\circ$  at the nadir.

We transformed retinal or visual field locations from spherical retinocentric coordinates to global mouse-centred coordinates using two key additional values. The first was the orientation of the optic axis in the head of ambulating mice, drawn from Oommen and Stahl<sup>40</sup>, namely at global mouse-centred coordinates (as defined here) of  $22^\circ$  elevation and  $64^\circ$  azimuth. These values accounted for the tilt maculo-ocular reflex (tiltMOR), which tilts the eye upward in visual space when the nose tilts downward. The second value was the torsional orientation of the eyes measured from the positions of the insertions of the lateral and medial rectus muscles relative to the stereotaxic lambda–bregma axis. To obtain this value, mice ( $n = 5$ ) were anaesthetized as for survival surgery, mounted in a stereotaxic apparatus, the skull exposed, and the mouse's head tilted about the interaural axis so that the lambda–bregma axis lay within a stereotaxic horizontal plane. Using a stereotaxically mounted fine probe as a depth guide, we used a cautery pen to make two small burn marks on the cornea, both within the same stereotaxic horizontal plane, but one at the rostral margin of the cornea, and the other at its caudal limit. The line connecting the two burn marks thus paralleled the lambda–bregma axis. We then measured the angle between this line and that connecting the insertions on the globe of the lateral and medial rectus muscles. This angle averaged  $35.6^\circ \pm 2.3^\circ$  (average  $\pm$  s.d.), with the medial rectus insertion lying above the lateral one.

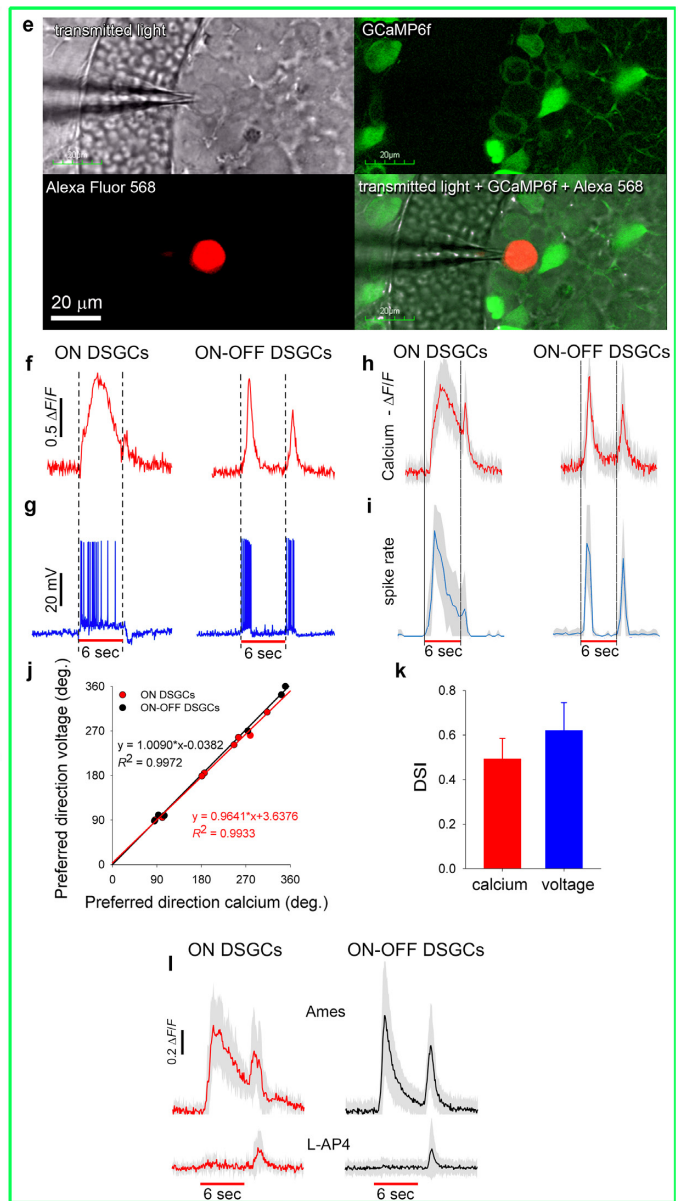
**Tomography of vestibular and ocular systems.** See Supplementary Methods and Supplementary Table 2.

**Data availability.** The data that support the findings of this study are available from the corresponding author upon request.

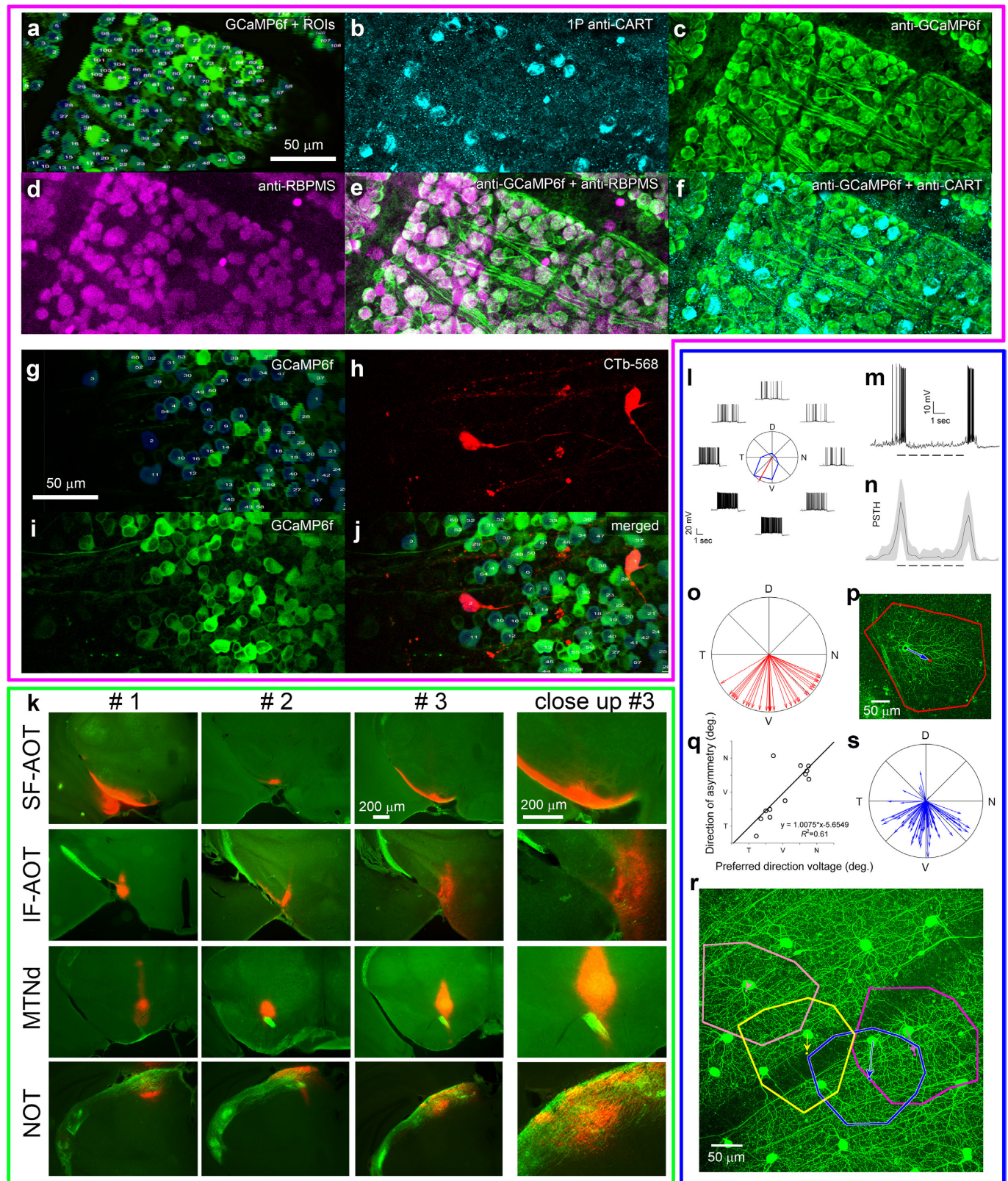
28. Ivanova, E., Toychiev, A. H., Yee, C. W. & Sagdullaev, B. T. Optimized protocol for retinal wholemount preparation for imaging and immunohistochemistry. *J. Vis. Exp.* e51018, <http://dx.doi.org/10.3791/51018> (2013).
29. Naarendorp, F. *et al.* Dark light, rod saturation, and the absolute and incremental sensitivity of mouse cone vision. *J. Neurosci.* **30**, 12495–12507 (2010).
30. Govardovskii, V. I., Fyhrquist, N., Reuter, T., Kuzmin, D. G. & Donner, K. In search of the visual pigment template. *Vis. Neurosci.* **17**, 509–528 (2000).
31. Szél, A. *et al.* Unique topographic separation of 2 spectral classes of cones in the mouse retina. *J. Comp. Neurol.* **325**, 327–342 (1992).
32. Dai, X. *et al.* The frequency-response electroretinogram distinguishes cone and abnormal rod function in *rd12* mice. *PLoS One* **10**, e0117570 (2015).
33. Borghuis, B. G., Marvin, J. S., Looger, L. L. & Demb, J. B. Two-photon imaging of nonlinear glutamate release dynamics at bipolar cell synapses in the mouse retina. *J. Neurosci.* **33**, 10972–10985 (2013).
34. Borghuis, B. G. *et al.* Imaging light responses of targeted neuron populations in the rodent retina. *J. Neurosci.* **31**, 2855–2867 (2011).
35. Kim, I. J., Zhang, Y. F., Yamagata, M., Meister, M. & Sanes, J. R. Molecular identification of a retinal cell type that responds to upward motion. *Nature* **452**, 478–483 (2008).
36. Chen, T. W. *et al.* Ultrasensitive fluorescent proteins for imaging neuronal activity. *Nature* **499**, 295–300 (2013).
37. Kass, R. E. & Raftery, A. E. Bayes factors. *J. Am. Statist. Assoc.* **90**, 773–795 (1995).
38. Venkataramani, S. & Taylor, W. R. Orientation selectivity in rabbit retinal ganglion cells is mediated by presynaptic inhibition. *J. Neurosci.* **30**, 15664–15676 (2010).
39. Maloney, L. T. Evaluation of linear-models of surface spectral reflectance with small numbers of parameters. *J. Opt. Soc. Am. A* **3**, 1673–1683 (1986).
40. Oommen, B. S. & Stahl, J. S. Eye orientation during static tilts and its relationship to spontaneous head pitch in the laboratory mouse. *Brain Res.* **1193**, 57–66 (2008).
41. Oh, S. W. *et al.* A mesoscale connectome of the mouse brain. *Nature* **508**, 207–214 (2014).
42. Yonehara, K. *et al.* Identification of retinal ganglion cells and their projections involved in central transmission of information about upward and downward image motion. *PLoS One* **4**, e4320, <http://dx.doi.org/10.1371/journal.pone.0004320> (2009).



**Extended Data Figure 1 | Direction selectivity of ON-DSGCs and ON-OFF-DSGCs revealed by their calcium and voltage responses.** **a–d**, Calcium transients of representative ON-OFF-DSGCs (**a, b**) and ON-DSGCs (**c, d**) in response to bright bars (**a, c**) or sinusoidal gratings (**b, d**) drifting in eight directions at 45° intervals. Preferred direction and direction-selectivity index (DSI) were determined from grating responses, cell class (ON-DSGC or ON-OFF-DSGC) from the bar responses. Traces plot somatic GCaMP6f  $\text{Ca}^{2+}$  signal over time (Methods); red shows mean; grey, single trials. Black marker indicates when stimulus bar was within the cell's receptive field. Polar plots show response amplitude (normalized to maximum) for each direction (bold curves, mean of four repetitions; thin, single trials). Red vectors show preferred direction (bold, mean; thin, single trials; N, nasal; D, dorsal; T, temporal; V, ventral). Direction-selectivity index (DSI) was higher for gratings than bars, especially for ON-DSGCs (Supplementary Note 9). **e–k**, Morphological and functional validation of DSGC subtypes inferred from  $\text{Ca}^{2+}$  imaging. **e**, GCaMP6f fluorescence (top right) revealed DS tuning in a cell that was then targeted for patch recording (top left) and



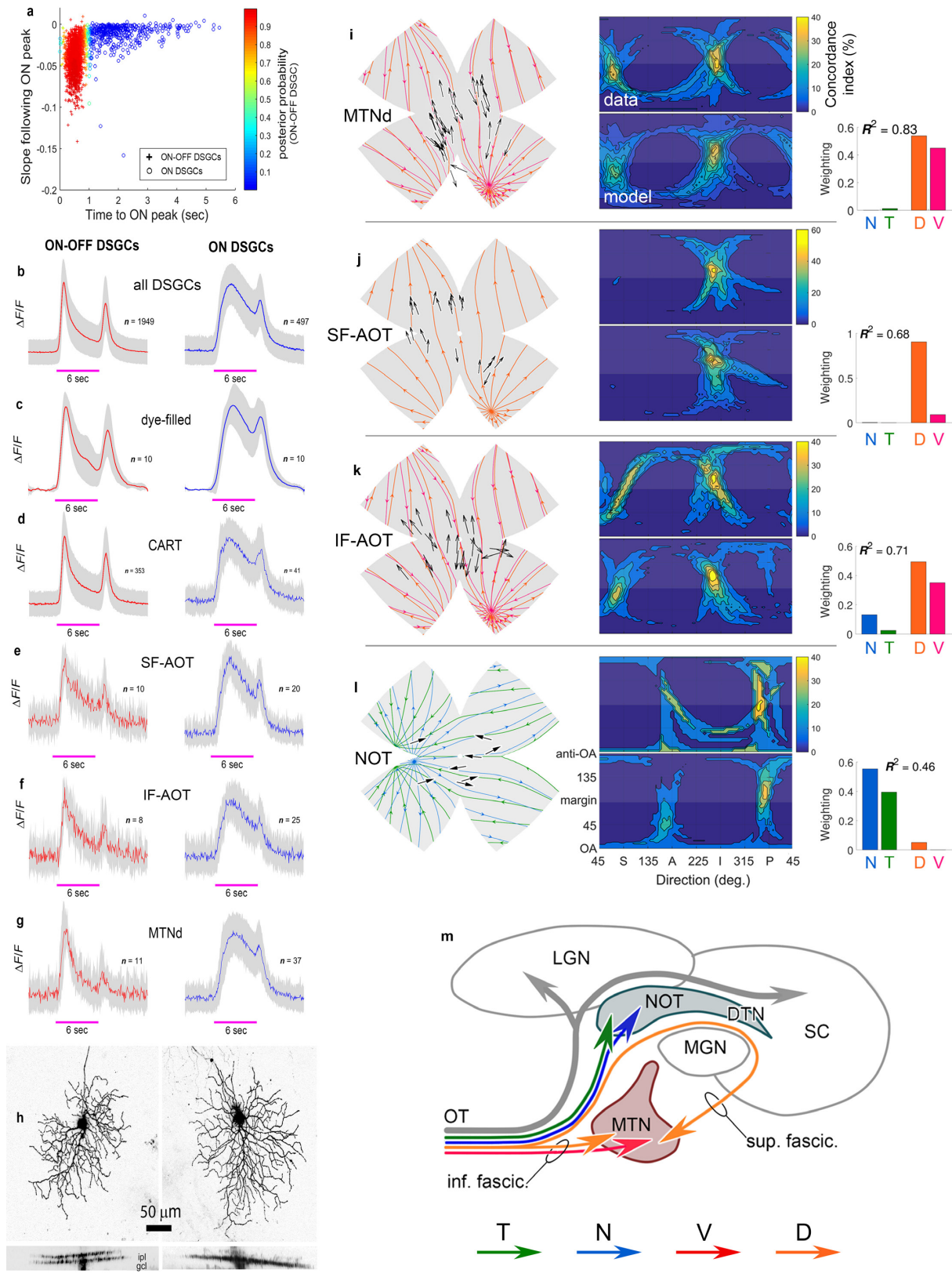
dye filling (bottom left; see Extended Data Fig. 3h for representative morphological data). **f, g**, Calcium (**f**) and voltage (**g**) traces for representative ON-DSGCs and ON-OFF-DSGCs in response to a drifting bright bar. **h, i**, Mean calcium responses (**h**) and peristimulus time histograms (PSTH) (**i**) for patched ON-DSGCs ( $n = 8$ ) and ON-OFF-DSGCs ( $n = 6$ ) in response to a drifting bright bar (grey bands:  $\pm 1$  s.d.). The bar's trailing edge evoked a small OFF  $\text{Ca}^{2+}$  transient in ON-DSGCs (**h**; see also **f**, left trace) and a very slight uptick in the PSTH (**i**). **j, k**, DS preference inferred from  $\text{Ca}^{2+}$  signal closely matches that inferred from spiking for both ON-DSGCs (red) and ON-OFF-DSGCs (black) (**j**), despite having significantly broader tuning (**k**; lower DSI; paired  $t$ -test,  $t = -4.068$ ,  $P < 0.001$ ). **l**, Bath application of a selective ON-channel blocker (L-AP4) abolished the ON response, but left an OFF transient of reduced amplitude in ON-DSGCs ( $n = 10$ ) and ON-OFF-DSGCs ( $n = 43$ ) alike. OFF responses of ON-DSGCs are presumably mediated by excitatory input from OFF bipolar cells to the sparse OFF dendritic arbors of ON-DSGCs<sup>22</sup>.



Extended Data Figure 2 | See next page for caption.

**Extended Data Figure 2 | Anatomical analyses.** Calcium is correlated with immunofluorescence, retrograde labelling and morphological asymmetries. **a–f**, Correlating  $\text{Ca}^{2+}$  imaging and post hoc immunofluorescence in a single imaged field. **a**, A two-photon image of GCaMP6f-expressing cells in live retina, *in vitro*. Numbers indicate regions of interest (ROIs) for assessing somatic DS responses. Cell-free zones are blood vessels. **b–f**, Confocal image of the same field after fixation, immunolabelling, and alignment with the live image (**a**). **b**, Immunolabelling for CART, a specific marker for 3 of 4 ON-OFF-DSGC subtypes (N-, V- and D-cells). **c**, Anti-GFP immunofluorescence, to enhance GCaMP6f signal which faded after fixation. **d**, Immunofluorescence for RBPMS, a marker for all RGCs. **e, f**, Merged images combining GCaMP6f (anti-GFP) signal with either RBPMS (**e**) or CART (**f**). **g–j**, Single imaged field demonstrating that identification of cells labelled by retrograde transport from the AOS can be linked to specific  $\text{Ca}^{2+}$ -imaged cells. **g**, Two-photon image of GCaMP6f fluorescence in live retina *in vitro*; ROIs marked as in **a**. **h, i**, Live confocal images of same field, showing (**h**) two cells retrolabelled from the MTNd (**h**; fluorescent cholera toxin beta-subunit, CTb) and GCaMP6f fluorescence (**i**). **j**, Merged image of **h** and **i**. **k**, Confocal images of coronal sections showing retrograde-tracer deposits (red) in 12 different mice, three mice each (#1–3) for four AOS targets (rows): superior fasciculus of the accessory optic tract (SF-AOT); inferior fasciculus of the AOT (IF-AOT); dorsal division of the medial terminal nucleus (MTNd); and nucleus of the optic tract (NOT). Far right column shows enlarged images from third column. These deposits spared retinorecipient nuclei outside the AOS, visible from nonspecific labelling by GCaMP6f fluorescence (green). **l–s**, Structure and

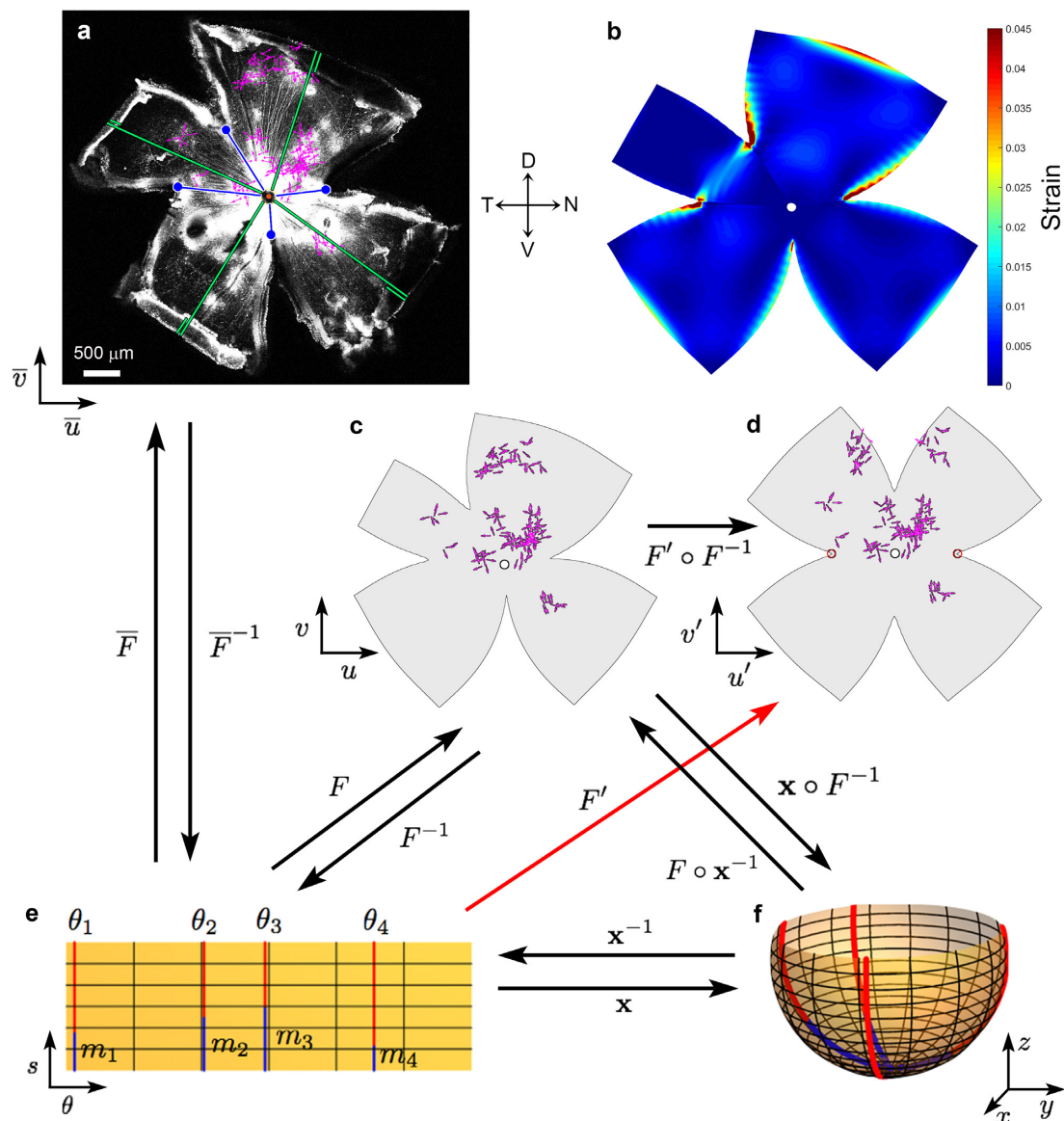
function of GFP-labelled DSGCs in Hb9-GFP mice. **l**, Voltage responses to drifting gratings (conventions as for Extended Data Fig. 1b, d). **m, n**, Spike responses to a bright bar moving in the preferred direction. Dashed line indicates roughly when the stimulus overlapped the receptive field. **m**, Voltage response of representative Hb9-GFP cell on a single trial. **n**, Mean peristimulus time histogram (PSTH) for all recorded Hb9-GFP cells ( $n = 32$ ; 4 retinas). Grey band represents  $\pm 1$  s.d. **o**, Preferred directions of all recorded GFP<sup>+</sup> cells ( $n = 32$  cells; 4 retinas). All point generally ventral, but scatter is substantial. (Arrow length not scaled to DSI). **p–s**, Dendritic asymmetry in Hb9 cells correlates with preferred direction. **p**, Typical Hb9 cell dye-filled during patch recording; maximum-intensity projected (MIP) confocal image. Blue vector indicates displacement of centroid of dendritic arbor (red dot) from the soma (black dot), a measure of the magnitude and direction of asymmetry. **q**, Dendritic asymmetry correlates strongly with physiologically determined DS preference ( $n = 12$ ). **r**, Assessment of dendritic-field asymmetry in Hb9-GFP cells based on GFP fluorescence alone. In this MIP image, coloured polygons show estimated dendritic-field envelopes for four cells. Vectors mark magnitude and direction of asymmetry as in **p**. **s**, Polar plot of direction and magnitude of dendritic asymmetry among a large sample of Hb9-GFP cells ( $n = 82$  cells; 3 retinas) estimated as in **r**. Estimates made blinded to retinal location. Vector length indicates magnitude of arbor asymmetry (displacement of dendritic-field centroid from soma, normalized by the arbor circumference). Nearly all markedly asymmetric fields were displaced in a ventral direction from their somatic location, but with substantial scatter.



Extended Data Figure 3 | See next page for caption.

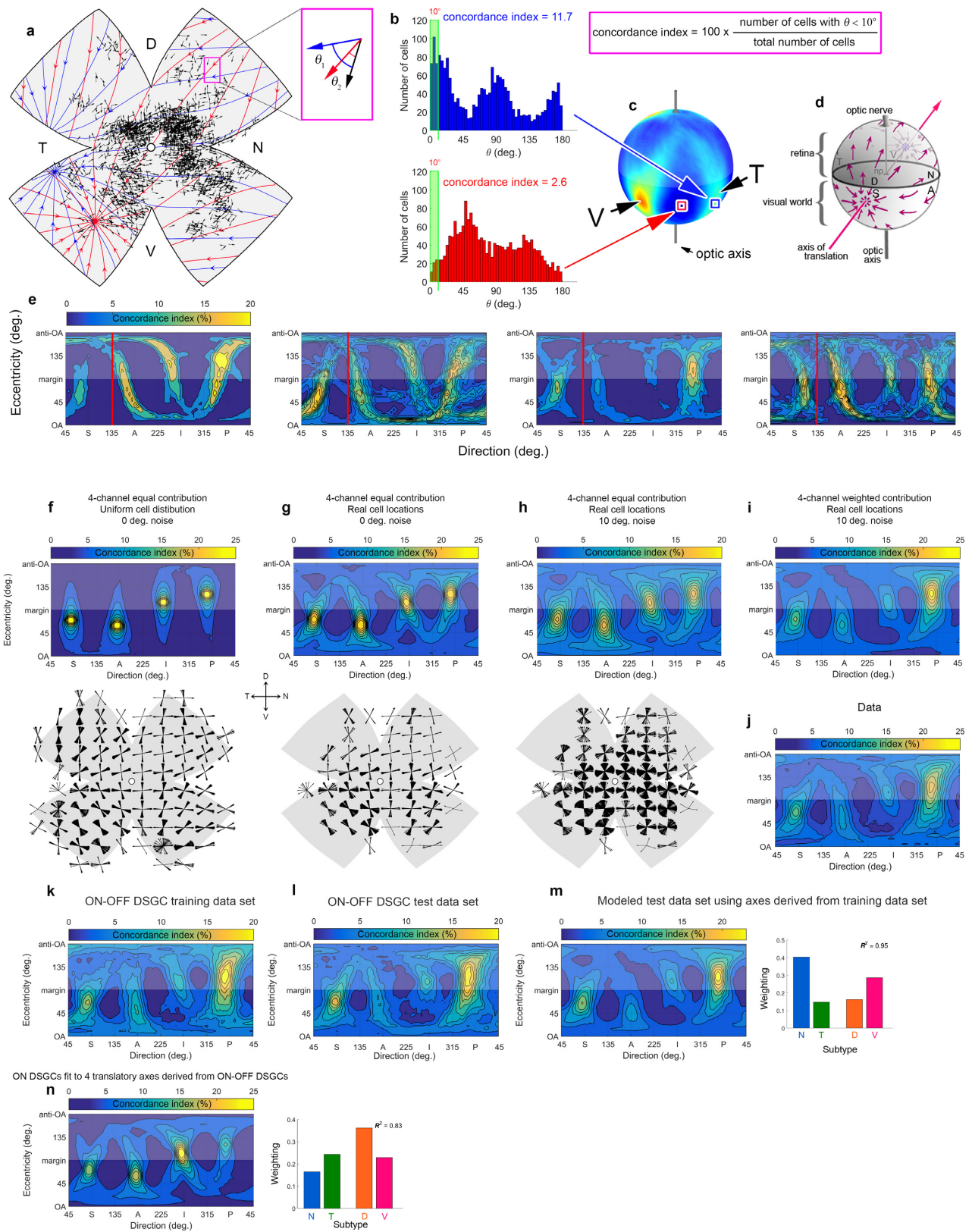
**Extended Data Figure 3 | Differentiation of ON-DGSCs from ON-OFF-DSGCs by unsupervised clustering and projections to accessory optic system.** **a**, DSGCs can be clustered into two classes (ON and ON-OFF) based on two parameters of  $\text{Ca}^{2+}$  responses to moving bars: (1) the latency of the ON peak (relative to the arrival of the bar at the receptive-field; assumes 300  $\mu\text{m}$  field diameter and accounts for cell position within the imaged field); and (2) the slope of decay for 300 ms following the ON peak, a measure of the transience. Each cell is shown by a point coloured to represent its posterior probability of belonging to the ON-OFF-DSGC cluster. Most cells are very likely to be one type or the other. **b–g**, Average  $\text{Ca}^{2+}$  signals ( $\Delta F/F$ ; mean (coloured line)  $\pm$  s.d. (grey area)) evoked by light bar moving in the preferred direction for various samples of DSGCs (ON-OFF-DSGCs: red traces; ON-DSGCs: blue): **b**, all imaged DSGCs; **c**, morphologically identified (dye-filled) DSGCs; **d**, CART-immunopositive DSGCs (comprising mainly N-, D-, and V-type ON-OFF-DSGCs); **e–g**, DSGCs retrolabelled from three components of the AOS: superior (**e**) and inferior fasciculi (**f**) of the AOT, and dorsal division of the MTN (**g**). See Supplementary Note 10 and ref. 41 for additional details. **h**, Representative morphology of ON-OFF-DSGCs (left)

and ON-DSGCs (right) revealed by dye injection after  $\text{Ca}^{2+}$  imaging, and illustrated as MIP confocal images, projected onto the retinal plane (top) and an orthogonal one (bottom). ON-OFF-DSGCs stratify about equally in ON and OFF sublaminae; ON-DSGCs mainly in the ON sublamina. **i–m**,  $\text{Ca}^{2+}$  imaging of retrolabelled cells shows ON-DSGC subtypes project differentially to AOS. Each panel includes DS preferences plotted on a standard flat retina with superimposed best-fitting optic flow for each subtype (left); translatory optic-flow-tuning plots (middle), one for the actual data (top) and a second for the best-fitting model (bottom); and model-derived weighting coefficients (right), providing an estimate of relative subtype abundance. D- and V-cells selectively innervated the medial terminal nucleus (MTN) (**i–k**), while T- and N-cells supplied the nucleus of the optic tract (NOT)/dorsal terminal nucleus (DTN) (**l**). The superior fasciculus of the AOT (SF-AOT) apparently carries only D-cell axons (**j**), whereas the inferior fasciculus (IF-AOT) and dorsal MTN (MTNd) contain mixed V and D fibres (**k**) (but see ref. 42). Thus, two cardinal translatory axes are separately represented in the AOS, one in the NOT/DTN and the other in the MTN.



**Extended Data Figure 4 | Mapping cell locations in standard retinal coordinates.** **a**, Representative experimental retina after GCaMP6f imaging (confocal image). Bright patches (mostly central) are GCaMP6f fluorescence. Magenta vectors show locations and DS preferences of imaged DSGCs. Four radial relieving cuts were made to promote flattening; blue circles mark their termini. The nasal and temporal cuts were made at medial and lateral rectus insertions; the line connecting these (the ‘horizontal reference line’) effectively parallels the horizontal plane in ambulating mice. Curl at retinal margins developed gradually and was taken into account. **b**, Map of estimated strain energy density, reflecting local stretching during flattening. **c–f**, Mapping of cell locations onto a standardized spherical coordinate system for pooling data across retinas and display in flattened (**d**) or hemispherical form (**f**). **c**, Data in **a** remapped into standardized spherical coordinates, followed by remapping into flattened form using modelled relieving cuts approximating the actual ones; close similarity to **a** indicates these transformations are accurate and reversible. **d**, Same as **c** but in the form of a standardized

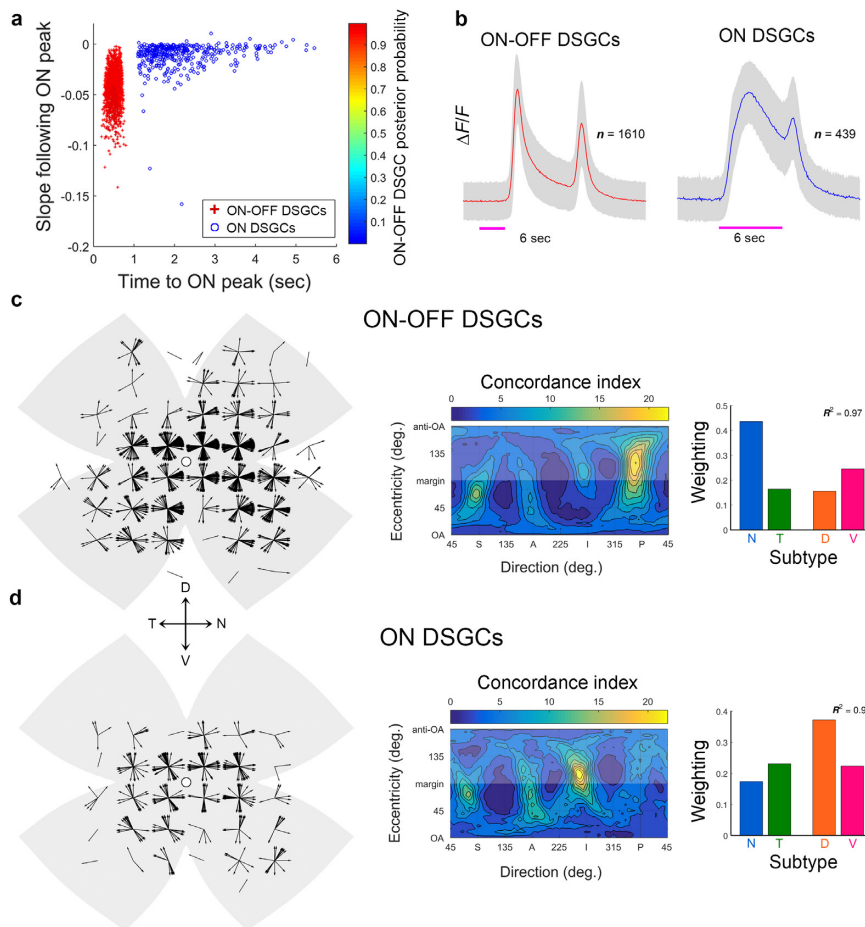
flat-mounted retina (four virtual radial cuts,  $90^\circ$  apart, extending 60% of the distance from retinal margin to optic disk). **e, f**, Schematic illustration of the mathematical approaches used for mapping to, and transformation between, coordinate systems. See Supplementary Equations for details. In **e**,  $s$  is arc length as measured from the optic disk;  $\theta$  is the longitudinal coordinate,  $0^\circ$  corresponds to the nasal terminus of the horizontal reference line,  $90^\circ$  to the dorsal retina, and so forth. Four red meridional arcs show the reconstructed positions of the four radial cuts in **a** and **c**. These have angular coordinates of  $\theta$ , and an arc length of  $M - m_i$ .  $M$  was approximated from the flat-mount as the average length of lines extending from the optic disk to the retinal margin (green lines, including the curled portions in **a**);  $m_i$  was estimated as the distance on the flat-mount from optic disk to the terminus of the corresponding radial cut (blue lines in **a**, **e** and **f**). Numerical reconstruction of the flat-mounted retina allowed empirical cell locations to be mapped to the spherical retina via the mapping  $\mathbf{x} \circ F^{-1}$ . Other mappings are shown on the double and single arrows.



Extended Data Figure 5 | See next page for caption.

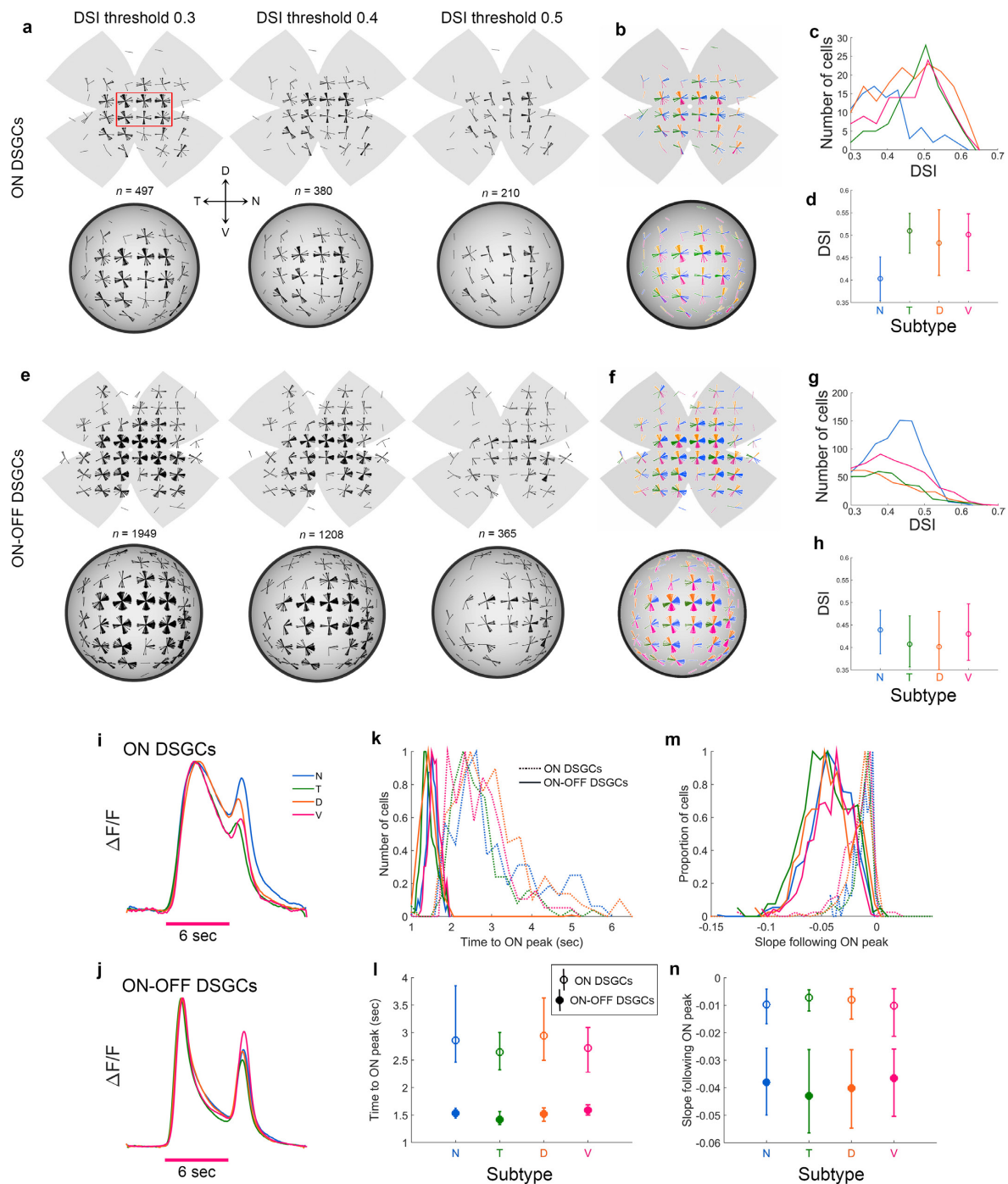
**Extended Data Figure 5 | Flow-tuning plots, correction for errors of rotatory orientation *in vitro*, and development of a flow-tuning model.** **a–d**, Generation of flow-tuning plots. **a**, DS preferences of all imaged ON-OFF-DSGCs mapped onto standard flattened retina. Each black vector marks one cell's location and preferred direction. How well do these DS preferences align with the local retinal optic flow produced by the mouse's translation along specific axes? Two flow fields are shown (blue and red lines and arrowheads); many more were tested (2,701 axes; 5° intervals of spherical angle). For each tested translation, we measured the angle  $\theta$  between each cell's preferred direction and the local direction of optic flow (inset:  $\theta_1$  for the blue flow field,  $\theta_2$  for the red one). N, nasal; D, dorsal; T, temporal; V, ventral. **b**, Distributions of angles  $\theta_1$  (top) and  $\theta_2$  (bottom) among all cells in **a**. Concordance index comprises the percentage of cells with DS preferences differing  $<10^\circ$  from the local motion in a specific flow field (green rectangles). Alignment was much greater with 'blue' than 'red' optic flow (concordance index = 11.7 and 2.6, respectively). **c**, Spherical translatory-flow-tuning plot displaying concordance index as a function of the axis of the animal's translation through space. Location of data for 'blue' and 'red' optic flows are indicated. **d**, Schematic representation of translatory optic flow induced in visual space (bottom hemisphere) and on retina (upper hemisphere) by animal's (and eye's) translation along the indicated axis (best axis of V-cell subtype). Translation along the indicated axis yields flow with a centre of contraction in the ventral retina (as for V-cells; Figs 1m and 2a) and in the corresponding locus in superior visual field. **e**, Correcting for errors of rotatory orientation of retina in chamber. Flattened translatory-flow-tuning plots for ON-OFF-DSGCs in four different retinas with large samples of imaged cells. Plots are highly stereotyped in form, but exhibit some variation in phase (that is, horizontal position; compare positions of hot spots to the arbitrary red

vertical reference line). To correct for this experimental error, we phase-shifted each retina's heat map (that is, offset it along the  $x$ -axis) to produce the best match with a reference heat map (an average of the four maps in **e**). See Methods for details. **f–i**, Stepwise development of the model of global DS geometry. Note the progressive improvement in the agreement between the flow-tuning plots of modelled and actual imaged ON-OFF-DSGCs (**j**). **f**, Basic version of the model. Modelled DSGCs were uniformly distributed over the retina. DS preferences set to local flow produced by translation in one direction along one of two orthogonal axes, derived in Fig. 3b. **g**, After restricting modelled cells to the locations of actual imaged cells. Smearing of hot spots reflects degraded certainty about the position of the best axes due to undersampling of cells in retinal regions near the singularities (centres of expansion or contraction). **h**, After mimicking biological and experimental variability by adding angular noise (standard deviation =  $10^\circ$ ) to the preferred directions of cells used in **g**. **i**, After accounting for the unequal abundances of subtypes by differentially weighting them before summation. Below: local polar plots of preferred directions of modelled DSGCs. Equivalent plots for cells in the final, refined model (**i**) are shown in Fig. 3j (black). **k–n**, Evidence for the predictive power of the model across data sets. ON-OFF-DSGCs were arbitrary divided into two samples, a training set (flow tuning plot in **k**) and a test set (**l**). Best translatory axes derived from the training set were used to generate a 4-subtype translatory flow-matching model of the same form as in **i**. **m**, flow-tuning plot for these modelled cells closely resembles that for imaged cells in the test set (**l**;  $R^2 = 0.95$ ). **n**, A model with translatory axes derived from ON-OFF-DSGCs predicts the DS preferences of imaged ON-DSGCs ( $R^2 = 0.83$ ). Weighting coefficients giving the best fit recapitulated those from direct modelling of ON-DSGC (Fig. 4j,m). See Supplementary Note 11 for details.



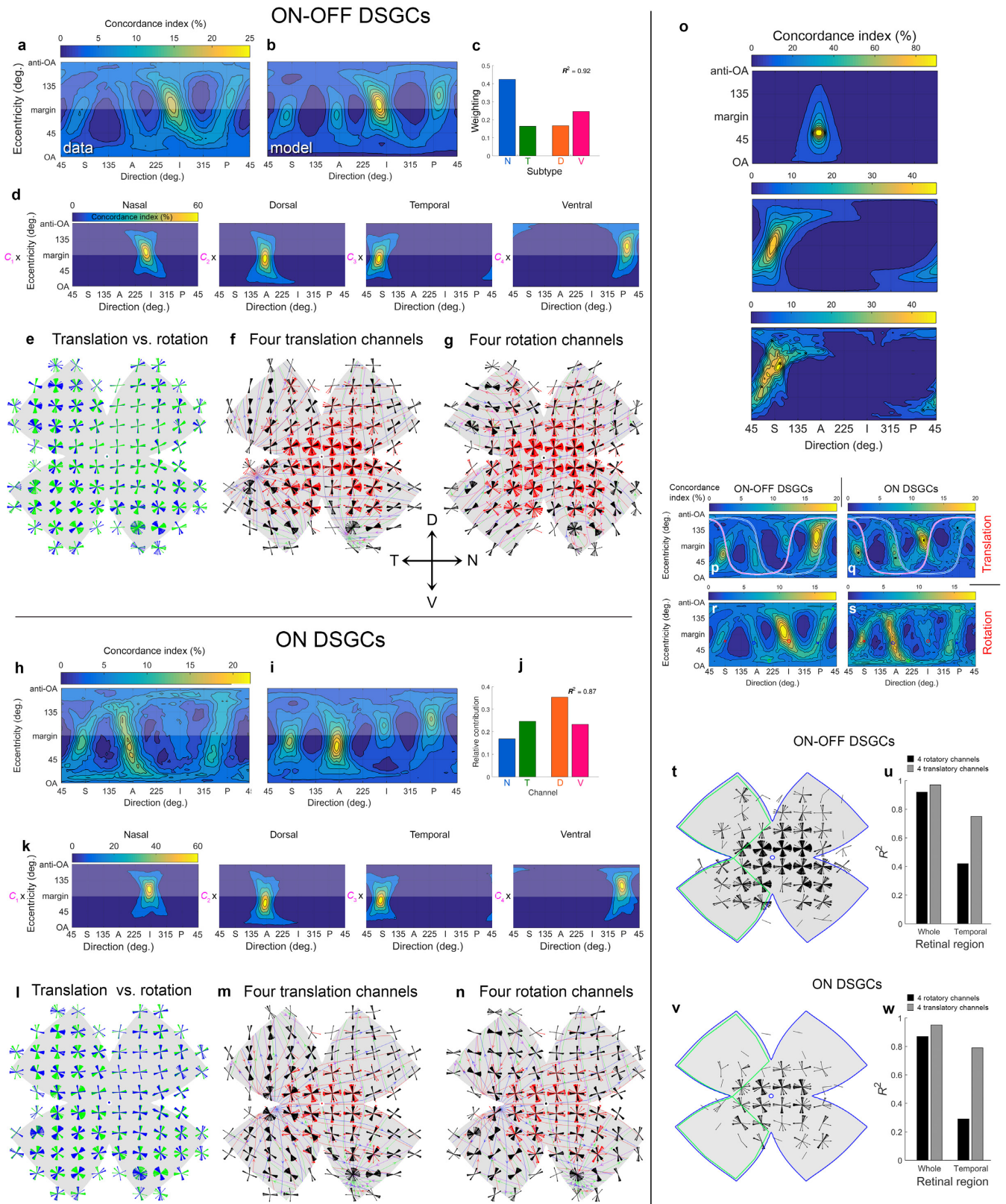
**Extended Data Figure 6 | Four ON-DSGC subtypes are still apparent when stringent criteria are used to distinguish them from ON-OFF-DSGCs.** Even when we apply a more stringent criterion to differentiate ON- from ON-OFF-DSGCs, we detect four ON-DSGC subtypes rather than the expected three (Fig. 4). **a**, Cluster analysis identical to Extended Data Fig. 3a but including only cells very likely to belong to the ON- or ON-OFF-DSGC classes (posterior probabilities  $>0.95$  of membership in one of the classes). This excluded 457 cells from analysis. **b**, Average calcium signals ( $\Delta F/F$ ; mean  $\pm$  s.d.) to moving bars for these stringently classified samples of ON-OFF-DSGCs (red traces) or ON-DSGCs (blue traces). See Extended Data Fig. 3b for details. **c, d**, Four subtypes remain

evident in both ON-OFF DSGCs (**c**) and ON DSGCs (**d**) and after application of the stringent classification criterion. These subtypes are evident in the four lobes of local polar plots of preferred direction (left) and in the four hot spots in the associated flattened translatory-flow-tuning plots (centre). Bar plots (right) display the weighting coefficients of the best fitting model, a measure of the relative abundance of the four subtypes. These weighting coefficients were similar to those obtained using the standard posterior-probability criterion ( $>0.5$ ), suggesting that the cells excluded due to the stringent criteria were distributed roughly equally across the four subtypes for each class.



**Extended Data Figure 7 | Selectivity for direction varies among DSGC subtypes.** **a**, Polar plots of local DS preference among ON-DSGCs, plotted on standard flat retinas (above) and in reconstructed hemispherical form (below). Increasing the stringency of the criterion for direction-selectivity index (DSI) from 0.3 to 0.5 reduced the number of N-cells (top left) by 95%, but other subtypes by only 42%–60% (sample zone: red rectangle). Thus, N-type ON-DS cells are unusually poorly tuned, and may have been excluded on that basis in previous studies reporting only three ON-DSGC subtypes. **b**, Leftmost panels of **a** reproduced with colour coded subtypes. Each cell's subtype assignment was determined by which of the four cardinal translatory flow fields was most closely aligned with its preferred direction. N, blue; T, green; D, orange; V, magenta. **c**, Line histograms showing the distribution of DSIs among each ON-DSGC subtype. The distribution for N-type ON-DSGCs is shifted to lower DSI values. **d**, Median DSI and first and third quartiles for each ON-DSGC

subtype. N-cells were significantly less well tuned. **e–h**, Same analysis as **a–d**, but for ON-OFF DSGCs. There were significant differences among subtypes but the stringency of the DSI criterion did not affect the relative abundance of subtypes. **i, j**, Mean calcium responses to preferred direction of bar motion of individual subtypes of ON-DSGCs ( $n = 497$ ) (**i**) and ON-OFF-DSGC ( $n = 1,949$ ) (**j**). **k, l**, Histograms (**k**) and mean values (plus first and third quartiles) (**l**) of latency to ON peak for each DSGC subtype, measured from estimated time of arrival bar edge at receptive field (see Methods). Latency differed significantly between each ON-DSGC subtype and its matching (homonymous) ON-OFF-DSGC subtype. **m, n**, Histograms (**m**) and median plus first and third quartiles (**n**) of the slope following the ON peak for each subtype of ON- and ON-OFF-DSGCs (see Methods). See Supplementary Note 12 for statistics and further details.

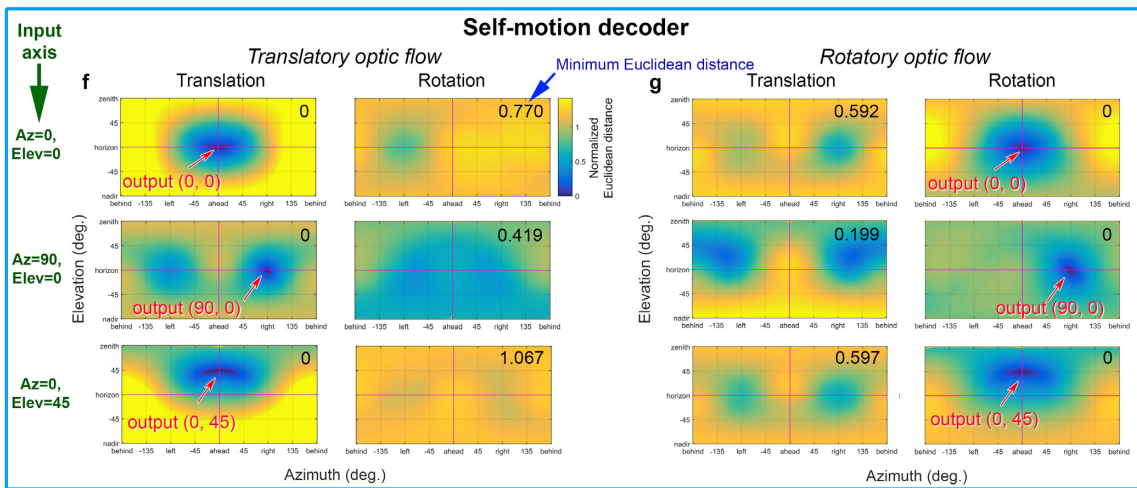
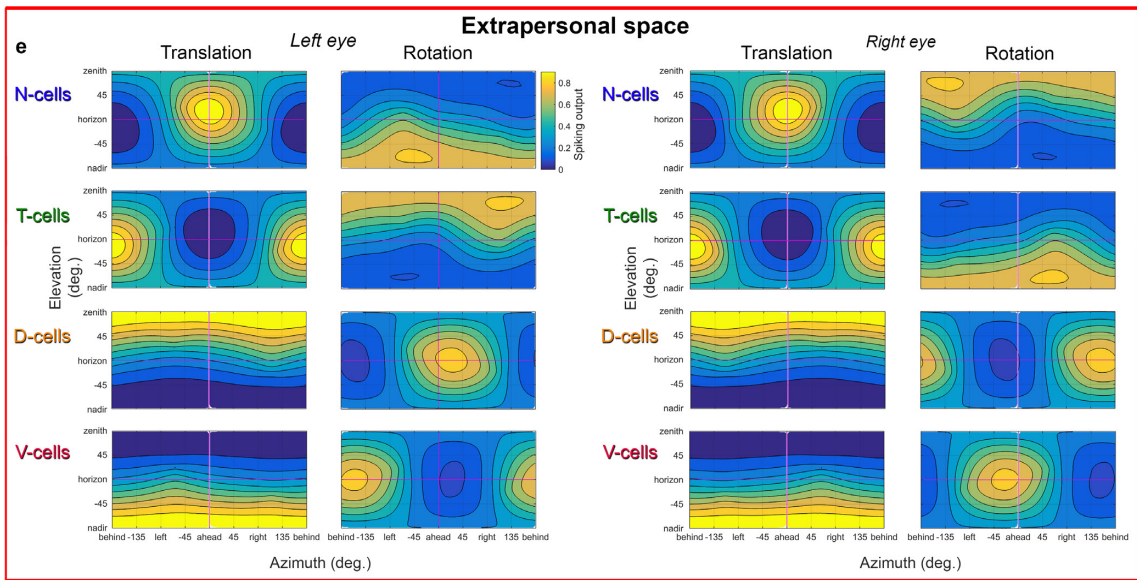
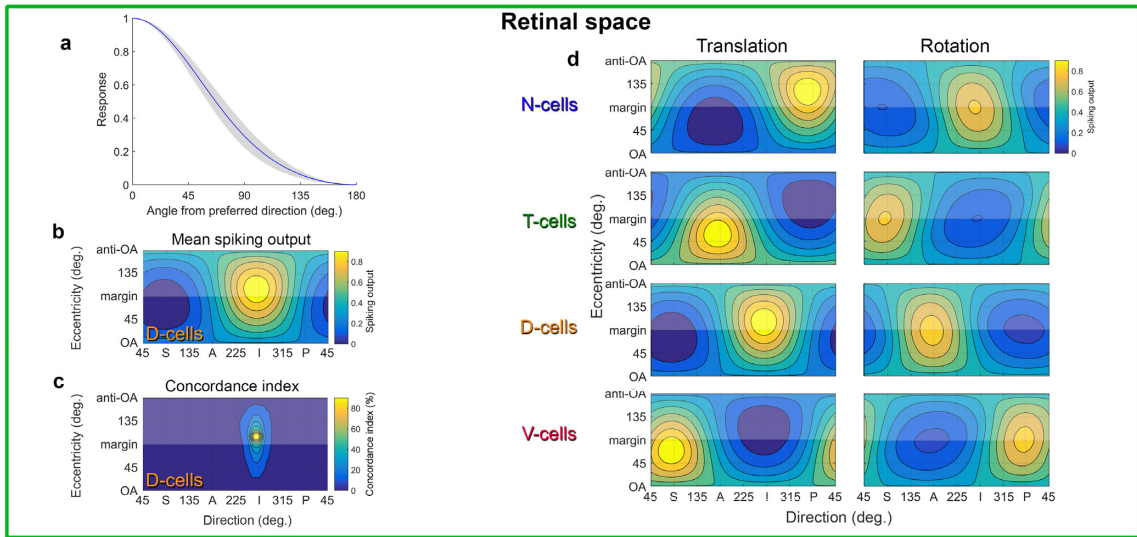


Extended Data Figure 8 | See next page for caption.

**Extended Data Figure 8 | Direction preferences of both ON-DSGCs and ON-OFF-DSGCs are better aligned with translatory optic flow fields than with rotatory ones.**

**a**, Flattened rotatory flow-tuning plot illustrating the concordance of DS preferences of all imaged ON-OFF-DSGCs with rotatory optic flow fields as a function of rotatory axis orientation (*plate carré* projection; compare Fig. 2j, k; Supplementary Note 13). **b**, Same as **a** but using modelled cells drawn from the best-fitting model. Model as for Extended Data Fig. 5i, but with subtypes (**d**) aligning DS preferences with rotatory instead of translatory optic flow fields (Supplementary Note 13). **c**, Weighting coefficients for the four subtypes in the best-fitting model. **d**, Rotatory-flow-tuning plots for the four individual rotatory-flow-matching subtypes used in the model, each with DS preferences aligned ( $\pm 10^\circ$  noise) with one of the four cardinal rotatory flow fields. **e–g**, Local polar plots of DS preferences predicted for two sets of modelled DS cells, aligning their DS preferences either with translatory optic flow (Fig. 3d–h) or with rotatory optic flow (this figure, **b** and **d**). **e**, Comparison of translatory and rotatory flow-matching models (green and blue polar plots, respectively). Predictions are similar in the central retina but diverge sharply in the periphery, especially ventrally and temporally. **f**, Observed preferred directions of imaged ON-OFF-DSGCs (red vectors;  $n = 1,949$ ) compared with those predicted by the model

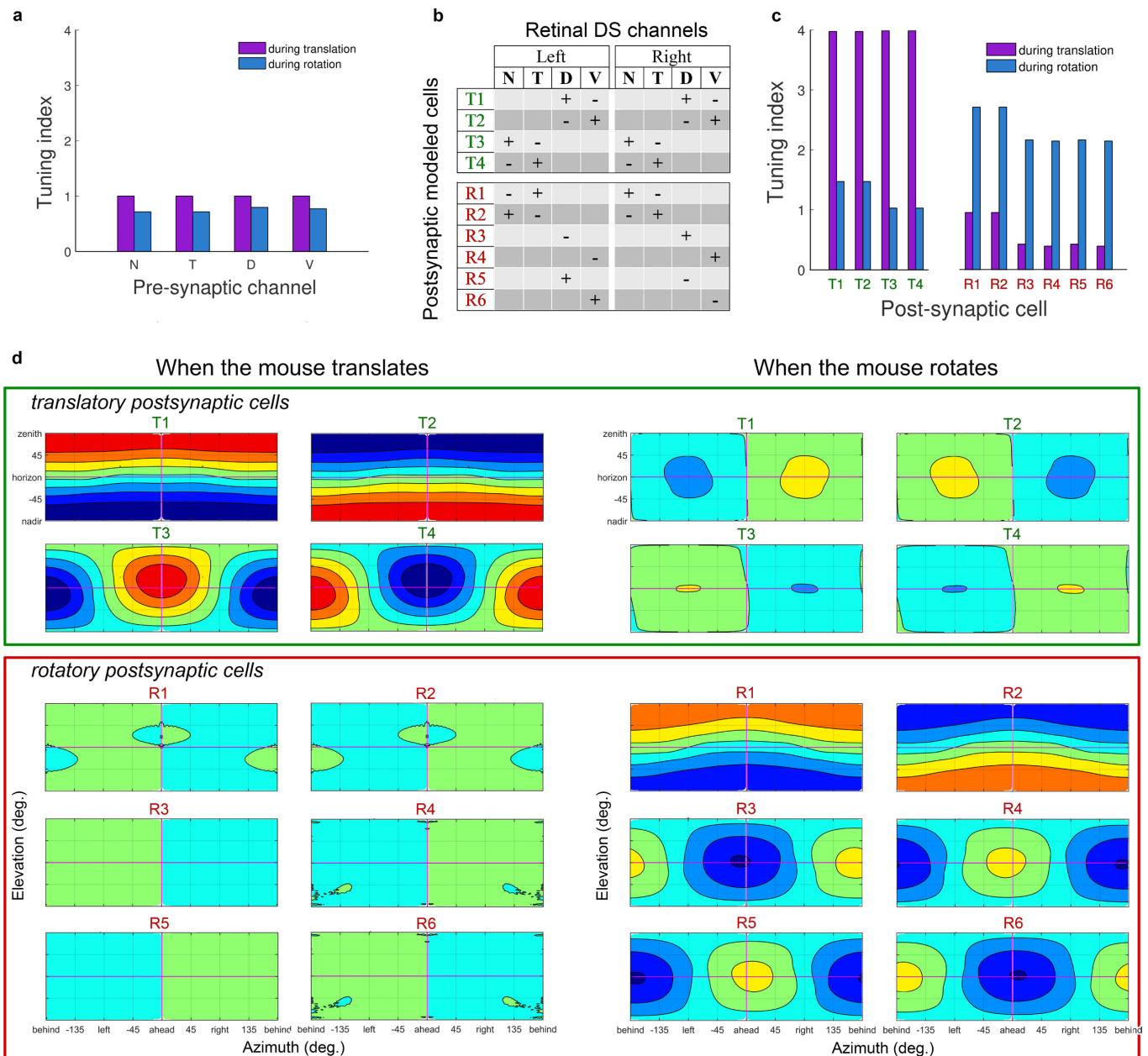
comprising four translatory-flow-matching channels (black vectors;  $n = 8,100$ ). **g**, Same as **f** but with preferred directions predicted from the rotatory-flow-matching model (black vectors;  $n = 8,100$ ). Optic flow preferred by each channel shown in pastel lines and arrowheads (N-cells, blue; D, green; T, red; V, magenta). **h–n**, Same as for **a–g** but comparing modelled and imaged ON-DSGCs. **o**, Comparison of real and modelled responses to translatory and rotatory flow for an ensemble comprising a single ON-OFF-DSGC subtype (T-cells). Modelled cells were aligned with their respective canonical translatory optic flows and were uniformly distributed over the retina. Top: response of modelled T-cell ensemble to translatory optic flow. Middle: modelled ensemble response of same cells to rotatory optic flow. Bottom: same as middle, but for real imaged T-cells. **p–s**, Flow-tuning plots for all imaged ON-OFF-DSGCs (**p**, **r**) and ON-DSGCs (**q**, **s**) probed with translatory (**p**, **q**) or rotatory (**r**, **s**) flow. **t–w**, Translatory-flow-matching model outperforms its rotatory equivalent overall, but especially temporally (green sector in **t** and **v**), where model predictions are most divergent (see **e**). **u**, **w**, Bar plots of  $R^2$  for fit to data of translatory (grey) and rotatory (black) models, assessed separately for the retina overall (left) or the temporal sample region alone. Similar trends were also apparent near the ventral translatory singularity (not shown).



Extended Data Figure 9 | See next page for caption.

**Extended Data Figure 9 | Ensemble coding by DSGCs of all possible translatory and rotatory optic flows, mapped in retinal or global coordinates.** **a**, Average directional tuning curve of imaged DSGCs (mean  $\text{Ca}^{2+}$  response, normalized to maximum, as a function of the angular offset from preferred directions). Tuning curves did not differ for ON- and ON-OFF-DSGC classes (see Methods). **b**, Flattened map of summed spike output of a single modelled ON-OFF-DSGC subtype—the D-cells—as a function of direction of the animal's translation, expressed in retinal coordinates. Hot spot indicates location in retinal space of the centre of contraction of the preferred translatory flow field (Supplementary Note 14). **c**, Alternative flow-tuning plot for the same subtype but plotting the concordance index (as elsewhere in this report; compare Fig. 2d–k; Supplementary Note 14). **d**, Flow-tuning plots of estimated summed ensemble spike output for each of four modelled translatory-flow-matching DSGC subtypes in response to optic flow generated by translation along (left column) or rotation about any axis (right column). **e**, Same as **d** but remapped in space and shown separately for the left and right eyes. Azimuth of zero is anterior; elevation of  $90^\circ$  is overhead. Hot spots in maps for translatory optic flow (first and third columns) indicate the best mouse-centred direction of heading for activating that DS subtype ensemble (Supplementary Note 14). **f, g**, Decoder model showing the brain could discriminate rotatory from translatory optic flow and identify the axis of self-motion by exploiting unique patterns of relative activation of the eight DS-channels

(4 subtypes  $\times$  2 eyes) induced by specific optic flow fields. **f**, Left column, heat plots showing, as a function of axis orientation, the Euclidean distance (dissimilarity) between two patterns of relative activation of the eight DS channels induced by: (1) translation along that axis; and (2) translation along a single 'input' axis (the unknown to be inferred by decoding, indicated at left, in green). Each probed axis is represented by a single pixel in the global map. Coldest colour marks the coordinates in space of the axis of translation evoking eight-channel outputs closest in Euclidean distance (black number, upper right), and thus highest in similarity, to the eight-channel outputs evoked by the reference (unknown) axis. Right column, same as left except that the eight-channel outputs induced by the input translatory optic flow are now compared to those of the same eight channels when induced by rotation about any possible axis. The coldest spot in this plot marks the orientation of the rotatory axis producing an 8-channel output pattern most similar to that produced by translation along the input (unknown) axis. **g**, Same as **f** except that the input axis listed at left (the unknown) is an axis of rotation, rather than of translation. In each case, the flow field generating eight-channel outputs most like those induced by rotation about the input axis (minimum Euclidean distance and darkest blue) is rotatory (right column of plots), not translatory (left column), and the orientation of the best-matching rotatory axis corresponds to that of the input axis of rotation. See Supplementary Note 14 for further explanation and interpretation.



**Extended Data Figure 10 | Modelled postsynaptic cells differentially tuned for rotation or translation are easily generated by summing or subtracting specific DS channels in the two eyes.** **a**, We devised a 'tuning index' to quantify the strength of tuning of single modelled subtype-ensembles for specific optic flow fields (Extended Data Fig. 9). The index consisted simply of the range of the Euclidean-distance values for the individual modelled DSGC ensembles. Individual DSGC subtype ensembles are nearly as well tuned to a specific axis of rotation as they are to their best axis of translation (Extended Data Figs 8a, h, 9e). **b**, Design of a simple model for generating postsynaptic cells with a selective preference for translation over rotation (T1–T4), or for rotation over translation (R1–R6), through linear summation or subtraction of multiple DSGC channels in the two eyes (see Supplementary Note 15 for details on model

design). **c**, Selectivity of modelled postsynaptic cell types for specific translations (T1–T4) or rotations (R1–R6), reflected in the tuning index as in **a**; note the enhanced ability to distinguish between translation and rotation relative to the input DSGCs (**a**). **d**, Flattened spherical ensemble-output plots, showing variations in net excitation of specific modelled postsynaptic cell classes as a function of the axis of translation or rotation, all in mouse-centred (global) coordinates (see Extended Data Fig. 9e). In heat maps, red and blue represent maximum and minimum channel activation, respectively. The model thus demonstrates that arithmetic combinations of signals from specific retinal DS channels could allow the brain to decompose optic flow into its translatory and rotatory components, paralleling the biomechanical decomposition of self-motion into these components by the vestibular labyrinth.